Self-Assembled Whispering Gallery Mode, Random and Distributed Feedback Biolasers

by

Itır Bakış Doğru-Yüksel

A Dissertation Submitted to the
Graduate School of Sciences and Engineering
in Partial Fulfillment of the Requirements for
the Degree of

Doctor of Philosophy

in

Biomedical Science and Engineering

KOÇ ÜNİVERSİTESİ

July 30, 2020

Self-Assembled Whispering Gallery Mode, Random and Distributed Feedback Biolasers

Koç University

Graduate School of Sciences and Engineering

This is to certify that I have examined this copy of a doctoral dissertation by

Itır Bakış Doğru-Yüksel

and have found that it is complete and satisfactory in all respects, and that any and all revisions required by the final examining committee have been made.

Committee Members:

Assoc. Prof. Sedat Nizamoğlu (Advisor)

Prof. Alphan Sennaroğlu

Prof. Alper Kiraz

Assoc. Prof. Onur Ferhanoğlu

Assoc. Prof. Serkan Ateş

Date: 30.07.2020

To Gökay and Lavi

ABSTRACT

Ever since their first demonstration by Theodore Maiman in 1960, lasers have enormous influence in our life. Laser light is coherent in space and time, directional and its spectrum is tunable. With their unique emission properties, lasers have a broad range of applications including barcode readers, blu-ray players, high-resolution imaging, and fiber-optic communication. Moreover, their use is emerging in biomedical imaging, diagnosis, and surgery. Commonly, lasers are fabricated using artificial or inorganic materials, however, these lasers are not proper to interface with living systems such as cells and tissues.

As a solution, in this research, we fabricated biomaterial-based lasers (biolasers) made of biocompatible materials of proteins and biopolymers. Motivating from the coffee-stain effect, we developed unconventional cavities for biolasers using self-assembly methods. First, we demonstrated whispering gallery mode biolasers using silk fibroin protein and synthetic biopolymers. No tools, components, and/or human intervention are needed after the construction process is initiated. In the first section, we showed the transition of 2D coffee stain into 3D hollow spheroid structure and utilized them spheroid lasers. Next, we used the suppression of the coffee stain effect to fabricate disk lasers that are flexible, physically transient, and can be directly integrated on a variety of substrates.

Second, we explained the use of self-assembled spatially localized feedback random lasers utilizing cracks. Directional random lasers with high Q-factors were presented using a wide variety of materials including fluorescent proteins, silk fibroin, silica nanoparticles, and synthetic biopolymers.

Finally, we stated single transverse mode all protein lasers utilizing distributed feedback cavities and the emission was adjusted according to the cavity design. Our findings introduce an innovative way of fabricating biocompatible and biodegradable lasers. This research generates the foundation of the advances of biolasers that are implantable to living systems.

ÖZET

1960 yılında Theodore Maiman tarafından ilk kez gösterilmesinden bu yana, lazerler hayatımızda oldukça önemli etkiler yaratmışlardır. Lazer ışığı uzay ve zamanda uyumludur, yönlüdür ve spektrumu ayarlanabilir. Bu benzersiz ışıma özellikleriyle lazerler, barkod okuyucular, blu-ray oynatıcılar, yüksek çözünürlüklü görüntüleme ve fiber optik iletişim gibi çok çeşitli uygulamalarda kullanılırlar. Dahası, biyomedikal görüntüleme, tanı ve ameliyatlarda lazer kullanımı artmaktadır. Genel olarak, lazerler yapay veya inorganik malzemelerden yapılır ancak bu malzemeler lazerlerin hücre ve dokulara temas etmek için uygun değildir.

Bir çözüm olarak, bu araştırmada, proteinler ve biyopolimerler kullanılarak biyomalzeme lazerler (biolazerler) ürettik. Biyomalzeme lazerleri üretebilmek için kahve lekesi etkisinden esinlenerek kendiliğinden oluşan ve bilinen yapılardan farklı kavite şekilleri geliştirdik. İlk olarak, ipek fibrin protein ve sentetik biyopolimerler kullanarak fısıldayan galeri modu biyolazerleri gösterdik. Üretim başladıktan sonra hiçbir aygıt, bileşen ya da insan etkisi ile yapılanmaya müdahalede bulunmadık. İlk kısımda 2B kahve lekesini 3B içi delik kürecik yapılara çevirdik ve bunları lazer olarak kullandık. Sonrasında ise kahve lekesi etkisini bastırarak esnek, fiziksel olarak geçici ve çeşitli yüzeylere aktarılabilen disk lazerler ürettik.

İkinci bölümde ise, kendiliğinden oluşan çatlaklar kullanarak mekansal olarak konumlandırılmış geri beslemeye dayalı rastgele lazerlerin kullanımını açıklanmıştır. Yüksek nitelik etmenine sahip yönlü rastgele lazerler silika nanoparçacıklar, floresan proteinler, ipek fibrin ve sentetik biyopolimerler kullanılarak sunulmuştur.

Son olarak, tek enine manyetik alan kipli tamamen protein lazerler ışımanın kavite tasarımına göre ayarlandığı geribildirim kaviteler kullanılarak bildirilmiştir. Sonuçlarımız biyouyumlu ve biyobozunur lazerler üretmenin yenilikçi bir yolunu ortaya koymaktadır. Bu araştırma canlı organizmalara implant edilebilecek biyolazerler geliştirmek için zemin hazırlamaktadır.

ACKNOWLEDGEMENTS

Foremost, I would like to express my sincere thankfulness to my advisor, Assoc. Prof. Sedat Nizamoğlu for his endless support and patience during my Ph.D. study and research. His enthusiasm enabled me to push beyond my self-imposed limits.

I would like to thank my thesis monitoring committee: Prof. Alphan Sennaroğlu and Prof. Alper Kiraz for their helpful suggestions throughout my Ph.D. Besides, I would like to thank the rest of my thesis committee: Assoc. Prof. Onur Ferhanoğlu and Assoc. Prof. Serkan Ateş for their valuable time.

My sincere thanks also goes to our dear collaborators: Assist. Prof. Matjaž Humar, Assist. Prof. Erkan Şenses, Prof. İskender Yılgör, Emel Yılgör, Assist. Prof. Çağla Koşak Söz, Prof. Tae-il Kim, Assist. Prof. Emir Salih Mağden, Assoc. Prof. Sunghwan Kim, Assist. Prof. Kyungtaek Min, Assist. Prof. Elif Nur Fırat Karalar, Dr. Byeonghak Park, Dr. Muhammad Umar, Deniz Çonkar, Efe Begar, Gregor Pirnat, Chanho Jeong and Ju Seung Lee.

I thank current and former *Idea*LAB members: especially to Mertcan Han, Houman Bahmani Jalali, Onuralp Karatüm, Asım Önal, Güncem Özgün Eren; they are like brothers to me and we had great times together. Also, I thank Dr. Daniel Aaron Press, Dr. Shashi Brushan Srivastava, Anıl Fettahoğlu, Rustamzhon Melikov, and Fatma Öz.

I would like to thank my friends I met in neighboring offices and now they are important part of my life: Serena Muratcıoğlu, Bilgesu Erdoğan, Nazlı Ataç, Efe Elbeyli, Özgün Can Önder, Gökhan Serhat, Yasemin Vardar and Ömer Kırnap.

I would like to thank my beloved family: my mother Nurcihan Güneşdoğan-Doğru, my father Musa Doğru, my brother Yusuf Doğuş Doğru, my sister-in-law Duygu Payzın-Doğru, and my lovely niece Yuna Doğru. I feel truly lucky to have such a loving and caring family.

Last but not the least, I would like to thank my boyfriend, best friend, husband, the love of my life, and everything: Gökay Yüksel. I thank my cat, Lavi, who tried to contribute to this thesis by sitting on the keyboard. Both of you are my home!

This thesis is supported by the Scientific and Technological Research Council of Turkey (TÜBİTAK) under projects 114F317, 115F451, 118E794, 117E177, 118E357,115E115, 115E242, 115F451, and 114E194, Marie Curie Career Integration Grant (PROTEINLED, 631679), European Research Council (ERC) under the European Union Horizon 2020 Research and Innovation Programme (grant agreement no. 639846) and the Turkish Academy of Sciences (GEBIP).

TABLE OF CONTENTS

LIST OF FIGURES

ABBREVIATIONS

AFM	Atomic Force Microscope
ASE	Amplified Spontaneous Emission
ATR	Attenuated Total Reflectance
BBO	Beta Barium Borate
BSDF	Bidirectional Scattering Distribution Function
CA	Contact Angle
DFB	Distributed Feedback
E. coli	Escherichia coli
eGFP	Enhanced Green Fluorescent Protein
FDTD	Finite Difference Time Domain
FSR	Free Spectral Range
FTIR	Fourier Transform Infrared Spectroscopy
FWHM	Full Width at Half Maximum
GFP	Green Fluorescent Protein
LHL	Laser Holography Lithography
LiBr	Lithium Bromide
MEK	Methyl Ethyl Ketone
Na_2CO_3	Sodium Carbonate
Nd:YAG	Neodymimum doped Yttrium Aluminum Garnet
OD	Optical Density
OPO	Optical Parametric Oscillator
PMMA	Poly (methyl methacrylate)
PTFE	Polytetrafluoroethylene
PVP	Polyvinylpyrrolidone
RIE	Reactive Ion Etching
Q	Q-factor
R6G	Rhodamine 6G
RhB	Rhodamine B
RL	Random Laser

RMS	Root Mean Square
SDF	Spatially Distributed Feedback
SEM	Scanning Electron Microscopy
SF	Silk Fibroin
SHPSU	Polydimethylsiloxane-Urea
SLF	Spatially Localized Feedback
TiO_2	Titanium Oxide
VSL	Variable Stripe Length
WCA	Water Contact Angle
WGM	Whispering Gallery Mode
WLI	White Light Interferometry

Chapter 1

INTRODUCTION

Nature is always charming in terms of self-made patterns and structures. It offers stability with the least amount of work. In nature, from snowflakes to pinecones, from viruses to seashells we ran into numerous structures that build themselves spontaneously. As the principles of spontaneously forming are understood, self-assembly has begun to be scientifically appealing since there is no need for sophisticated devices and complex engineering steps. Self-assembly can appear with constituents from the molecular scale to meters [1]. For instance, the self-assembly of nano-rod arrays into the nano-sphere in Figure 1.1-a shows different electronic and optical properties than its components and shows a new type of functional material [2]. Micron-scale wrinkled microspheres spontaneously formed by silica nanoparticles in Figure 1.1-b and the grooves of wrinkles are used to trap particles [3]. Moreover, by mimicking the molecular interactions, millimetric hexagonal arrays are formed by capillary action as shown in Figure 1.1-c [1].

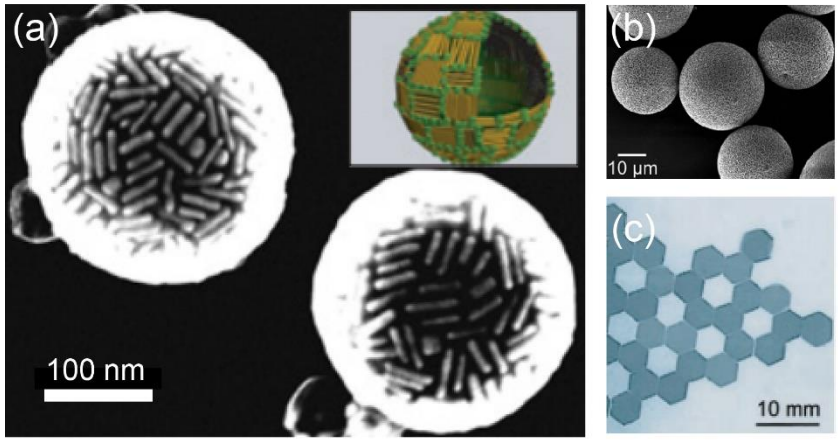

Figure 1.1 (a) Nano-spheres [2], **(b)** wrinkled microspheres [3], and **(c)** millimetric hexagonal arrays [1] formed by self-assembly methods.

To make self-assembled lasers, we inspired by the coffee stain effect. Coffee stain forms when a droplet of a colloidal solution dries on a surface [4]. A droplet of a colloidal solution spilled on a surface forms a spherical cap shape by surface tension. The contact area pins to the surface. Since the height of the perimeter is thinnest, evaporation is faster at the edges. The evaporated amount is replenished by the capillary flow carrying the particles inside it as shown in Figure 1.2. The particles deposited at the edges act as a barrier. After the solvent evaporates completely, the coffee ring forms along the perimeter of the droplet (Figure 1.3).

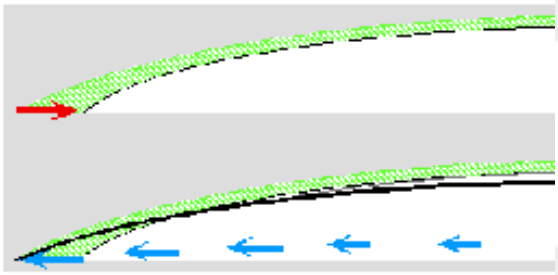

Figure 1.2 Outward flow mechanism during evaporation [4].

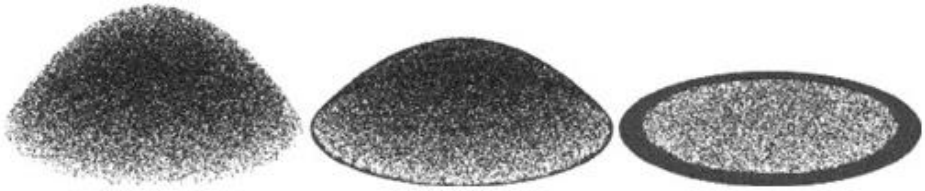

Figure 1.3 Schematic of coffee ring formation [5].

Previously, the coffee ring effect is utilized to arrange quantum rods[6], and nanorods [7] and lasing of the arranged rods were demonstrated. In another study, coffee rings made up of fluorescent proteins (Figure 1.4-a) are used as ring biolasers [8].

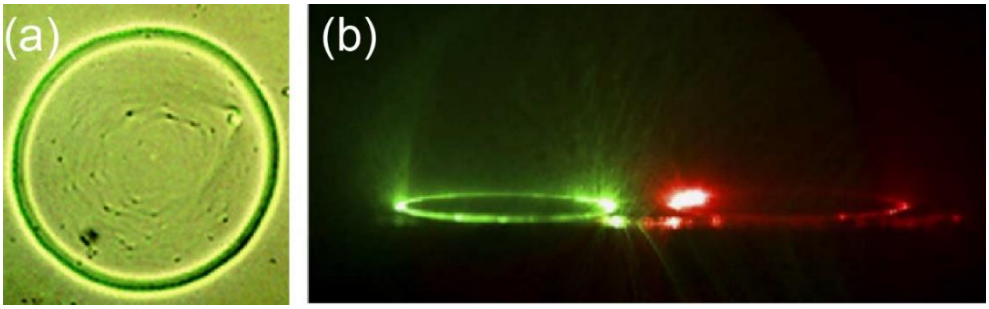

Figure 1.4 (a) Fluorescent protein coffee ring and **(b)** lasing of rings [8].

In this thesis, we developed self-assembled biolasers from organic dye or fluorescent protein doped colloidal solutions. Unlike previous studies, we created resonators based on the phenomenon of coffee stain but different from rings. The organization of the thesis is:

In the first chapter, we make a brief introduction about self-assembly, in particular the coffee stain effect.

In the second chapter, we briefly explain the working principles of lasers. Then, we state a common type of lasers in terms of their optical resonator design.

In the third chapter, we explain the experimental methods used in this research. First, we describe the synthesis of aqueous silk fibroin solution that is biocompatible, biodegradable, and mechanically robust. Then, we give details about the optical set-up used in the biolaser experiments.

The fourth chapter is about self-assembled whispering gallery mode resonators made up of silk fibroin proteins and biopolymers. We examine the self-assembly effect in terms of surface and heat. With these interventions, we obtained disk and spheroids and show their lasing emission.

In the fifth chapter, once again using coffee stain phenomena, we fabricated cracks and we demonstrate rough crack sidewalls are highly scattering and useful as random laser cavities.

In the sixth chapter, we state the single transverse mode and all protein lasers utilizing distributed feedback lasers.

In the last chapter, we close the thesis with future applications.

Chapter 2

LASER PHYSICS

Laser is an acronym for *Light Amplification by Stimulated Emission of Radiation.* To understand the working procedure of a laser, we need to understand each phenomenon that constitutes this acronym. In this chapter, stimulated emission, population inversion, and photon amplification is explained. Moreover, laser types in terms of optical cavities are briefly described.

2.1 Stimulated Emission

Absorption is a phenomenon that is observed when electromagnetic waves transmit their energy into a matter. An electron in an atom with initial state energy E_1 jumps to a state E_2 through its interaction of a photon with $h\nu=E_2-E_1$ energy is called absorption [9] as shown in Figure 2.1.

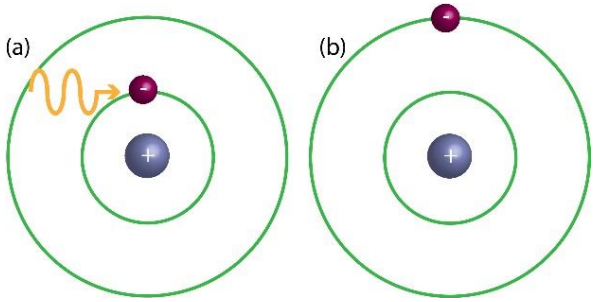

Figure 2.1 (a) Absorption of a photon and **(b)** excitation of an electron to a higher state.

The excited atom has a certain lifetime and when it jumps back to the lower state, it emits a photon as demonstrated in Figure 2.2. The released photon energy is equal to the energy difference between two states and the photon moves in a random direction and this phenomenon is nominated spontaneous emission [10].

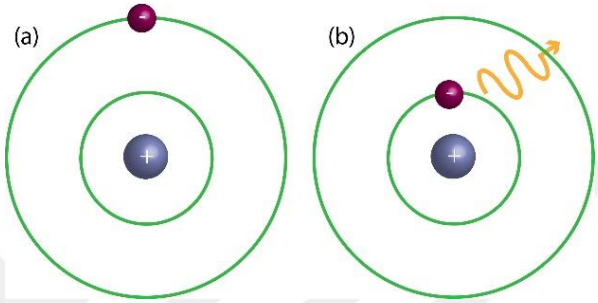

Figure 2.2 (a) Excited electron and **(b)** its fall to the lower state and spontaneous emission.

When a photon with $h\nu=E_2-E_1$ energy encounters with an excited electron at E_2 level, it perturbs the electron, the electron falls to E_1 state and emits a photon has the same frequency, phase, and polarization with the incoming photon. This process called stimulated emission [9], the passing electromagnetic wave leaves the atom increasing its energy one quantum ($h\nu$) as the two leaving photons are coherent with each other (Figure 2.3). When we avalanche this process, we obtain coherently amplified light that is one of the essentials to build a laser.

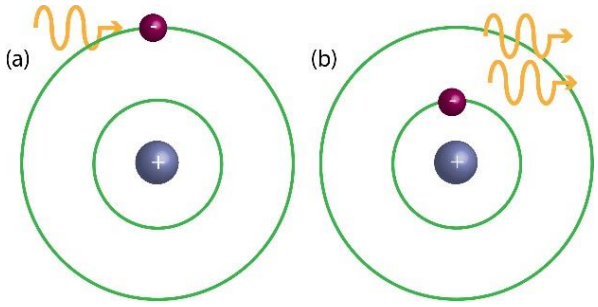

Figure 2.3 (a) Excited electron and **(b)** its stimulated emission through an incoming photon.

2.2 Population Inversion

Another requirement to build a laser is the population inversion. Population inversion occurs when there are more atoms at the higher state than the lower state. To acquire amplification, the number of incoming photons that stimulates the atom should dominate the number of incoming photons absorbed. However, population inversion cannot be achieved by two energy-level atoms.

To get population inversion, a metastable state that has slightly lower energy than the excited state can be utilized. E_1, E_2 and E_3 represent the energy levels of a three-level system in Figure 2.4. Considering when the electrons at the ground state are pumped to E_3 level via an external light source (Figure 2.4-a), they will rapidly decay to E_2 level and emit phonons (Figure 2.4-b). E_2 is a long-lived state, population inversion between E_2 and E_1 is more likely to happen. When a spontaneously emitted photon arrives at the electrons at E_2 state from the neighboring atoms (Figure 2.4-c), it stimulates the electron and we observe photon amplification, so-called optical gain (Figure 2.4-d).

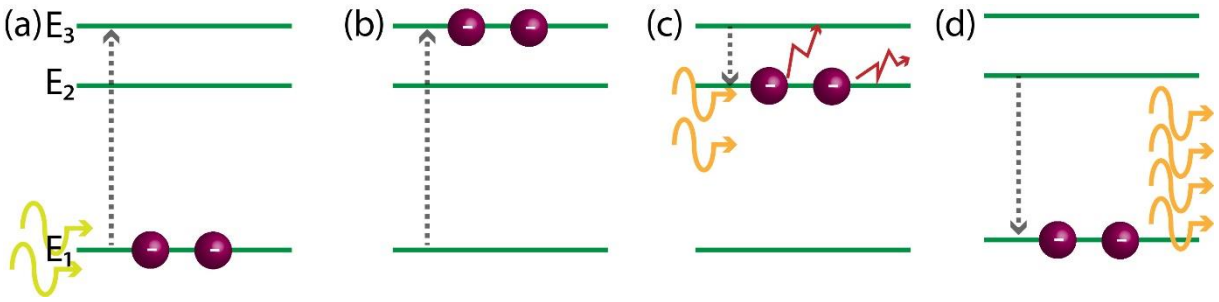

Figure 2.4 Working principle of three-level laser. **(a)** Pumping of electrons from the ground state to E_3 state. **(b)** Quick decay from E_3 to E_2 with phonon emission. **(c)** Population inversion between E_3 and E_2 and **(d)** stimulated emission.

Furthermore, there are four level laser systems with additional metastable are seen (Figure 2.5). In these systems, external photons pump the electrons from the ground state to E_3 state and electrons fast decay to long-lived E_2 state with phonon emission. After stimulation

electrons arrive to E_1 level, and quickly return back to ground level that is slightly below. In these system, population inversion between E_2 and E_1 is procured with lower pump power than three level energy systems.

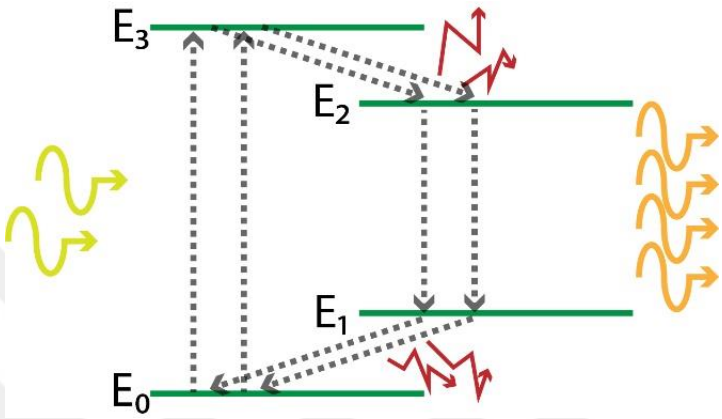

Figure 2.5 Working principle of four energy level laser

2.3 Photon Amplification

To construct a laser, another requirement is optical resonators. Optical resonators cause light to circulate in a closed path. When a gain medium inserted in a cavity, the emitted light by gain takes round trips by reflecting from resonator boundaries. At each turn, the reflected light stimulates the gain medium therefore resonators create an avalanche effect of stimulated emission and provide feedback. If the light constructively interferes with itself after one trip, it forms a standing wave and photon amplification is observed. If we say the length of the one trip is *l*, to support constructive interference, the wavelength λ should support

$$m\lambda = l \tag{2.1}$$

formula, where m is an integer and called mode number. The most commonly used lasers according to their optical resonator types are explained below.

2.3.1 Fabry–Pérot Lasers

Fabry–Pérot optical cavities are the simplest design of laser cavities that consist of two parallel mirrors facing each other [11]. One of the mirrors partially reflective to provide laser beam output after amplification. When the gain medium surrounded by the mirrors pumped, spontaneously emitted photons will initially travel in a random direction (Figure 2.6-a) and the ones move perpendicular to the mirrors are reflected back (Figure 2.6-b). They move back and forth reflecting the mirrors and stimulate the gain medium at each pass (Figure 2.6-c). The stimulated emission quickly amplifies when they interfering with each other. As a result, we obtain a standing wave (Figure 2.6-d). If we say the distance between two mirrors is L, and n is the refractive index, for Fabry–Pérot cavities one round trip is

$$l = 2nL \tag{2.2}$$

and the wavelengths that fit the Fabry–Pérot cavities can be found using Equation 3.

$$\lambda = 2nL/m \tag{2.3}$$

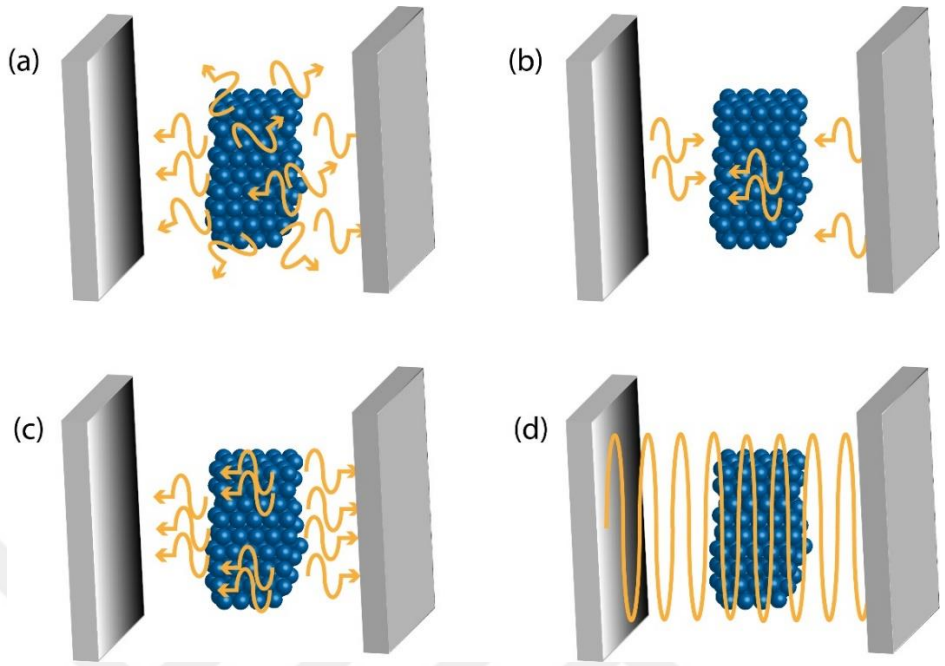

Figure 2.6 (a) Spontaneous emission in random directions when the gain medium is pumped. **(b)** Reflection of light waves from the mirrors and **(c)** stimulation of them as they move back and forth along the gain medium. **(d)** The standing wave formed by the stimulated photons constructively interference with themselves.

2.3.2 Whispering Gallery Mode Lasers

Whispering gallery mode (WGM) cavities confine the light by total internal reflection (TIR) [12]. The guided light wave circles by reflecting from the cavity surface (Figure 2.7-a) and when it constructively interferes with itself, it forms a standing wave (Figure 2.7-b). So toroids, disks, rings and spheres are suitable structures to be used as WGM resonators. To meet the resonance criteria in WGM resonators, if we say one round trip length

$$l = 2\pi nR \tag{2.4}$$

where R is the radius of the WGM cavity, the wavelengths should satisfy Equation 2.5.

$$\lambda = 2nR/m \tag{2.5}$$

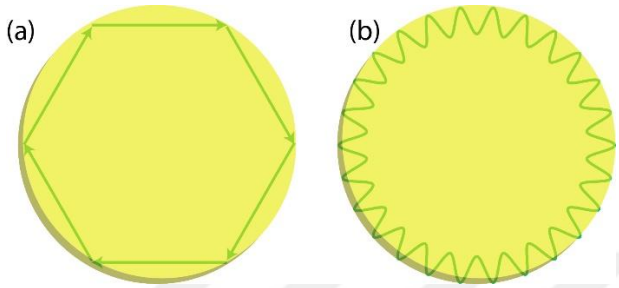

Figure 2.7 (a) Guided light in a WGM cavity by TIR and **(b)** its forming a standing wave.

2.3.3 Distributed Feedback Lasers

Distributed feedback (DFB) resonators are made up of periodic corrugated structures [10]. There is diffraction grating in their active region functions as Bragg reflector. Figure 2.8 shows a schematic of a DFB laser where a gain medium is inserted on top of the active region. When DFB is pumped, if two reflected waves from different corrugations constructively interfere, they amplify. To interfere, waves should be in phase when they meet. To maintain these criteria, their path difference should be an integer multiple of the wavelength. If we say that the Λ is the grating period length, the optical path difference reflected from two consecutive corrugations is 2Λ (light moves to the second corrugation and reflects). Therefore, the condition of in-phase interference is

$$q\,\lambda_B = 2n\Lambda \tag{2.6}$$

where n is the effective refractive index, q is the integer called diffraction order and λ_B is the Bragg wavelength. According to this formula, the emission wavelength of the DFB laser can be adjusted by period length. Only the wavelengths that support Formula 6 will lase, while

other wavelengths are suppressed by the resonator. This selective reflecting in DFB lasers results in single-mode emission.

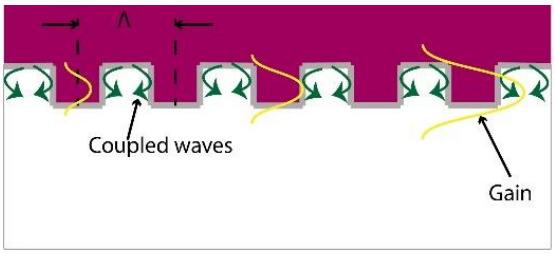

Figure 2.8 Schematic of DFB lasers

2.3.4 Random Lasers

Unlike the lasers mentioned above, random lasers (RLs) do not have a specific cavity. Instead of regular cavity design, there are randomly distributed scattering elements to provide optical feedback [13, 14]. The emitted photons travel along with the gain medium multi-scatters from the edges of irregular shapes or disordered particles as shown in Figure 2.9. The combination of scattering points forms a closed loop for the beam operating like a cavity [15]. The increase in the number of scattering elements traps the light inside the medium for a longer time and the beam amplifies during its travel [16]. The scattering points may be an irregular part of the gain medium like ridges and cracks or can be found independently dispersed in the gain medium [17]. Since the scattering is based on disordered and random arrangement, there is no need for controlled fabrication methods in RLs.

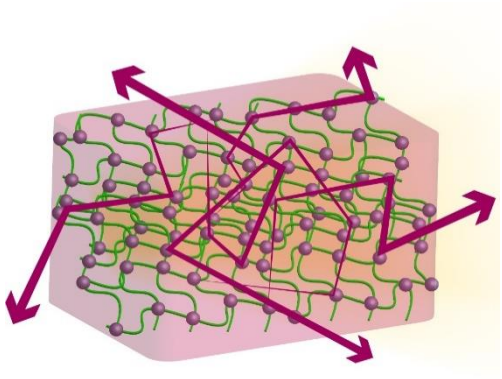

Figure 2.9 Schematic of scattering feedback based RL.

RLs based on scattering elements where they are randomly positioned is called RLs with spatially distributed feedback (SDF) as shown in Figure 2.9. Recently, a new architecture has been proposed where the gain medium is separated from the scattering region [18]. These RLs are called spatially localized feedback (SLF) based RLs. Their structure is quite similar to Fabry–Pérot lasers where the reflective mirrors are replaced by scattering surfaces as shown in Figure 2.10.

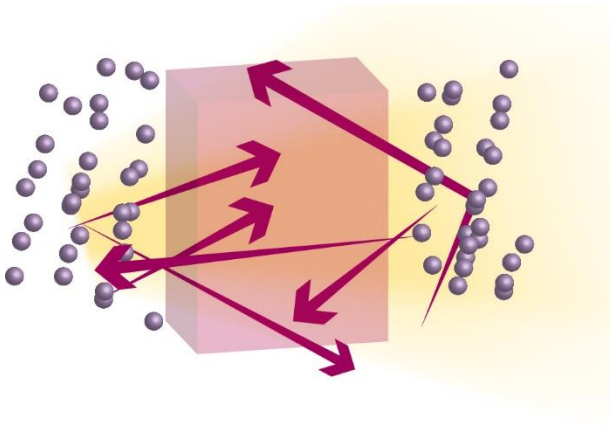

Figure 2.10 Schematic of SLF based RLs.

Chapter 3

MATERIALS & METHODS

3.1 Biomaterial Extraction

3.1.1 Preparation of Aqueous Silk Fibroin Solution

Silk fibroin (SF) is a natural protein that is directly extracted from *Bombyx Mori* silk cocoons (Figure 3.1-a). In this research, to make protein lasers, we utilized SF. Raw silk consists of sericin and fibroin proteins as demonstrated in the scanning electron microscopy (SEM) image in Figure 3.1-b. Fibroin proteins form the structural element of silk while sericin acts as a glue and hold the SF proteins together.

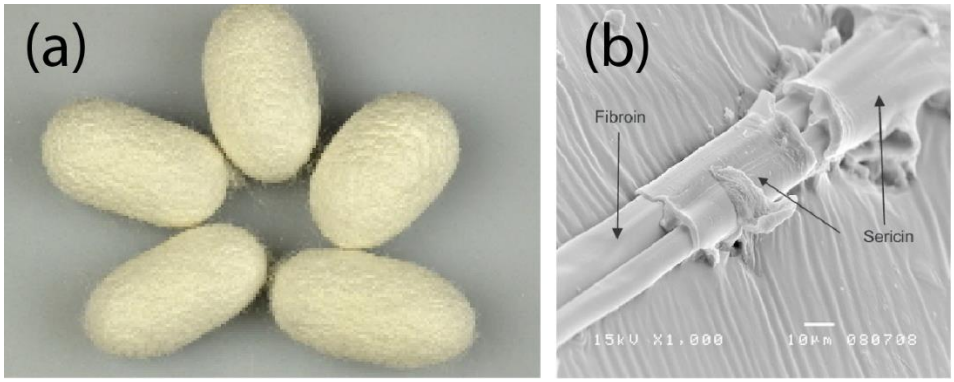

Figure 3.1 (a) Silk cocoons. **(b)** SEM image of silk fiber [19].

To extract SF, we need to remove sericin. First, we cut the cocoons into small pieces to remove the worms and increase the surface area (Figure 3.2-a). 4.24 g sodium carbonate (Na_2CO_3) is added to 2 liter boiling water to prepare 0.02 M aqueous Na_2CO_3 solution and 5 g cut cocoons are added (Figure 3.2-b) and stirred for half an hour to remove sericin using a

magnetic stirrer (Figure 3.2-c). Rinsed degummed SF is held in deionized water for 20 minutes and stirred (Figure 3.2-d). This process is repeated by changing the water. Afterward, SF is squeezed out (Figure 3.2-e) and allowed to dry at room temperature (Figure 3.2-f).

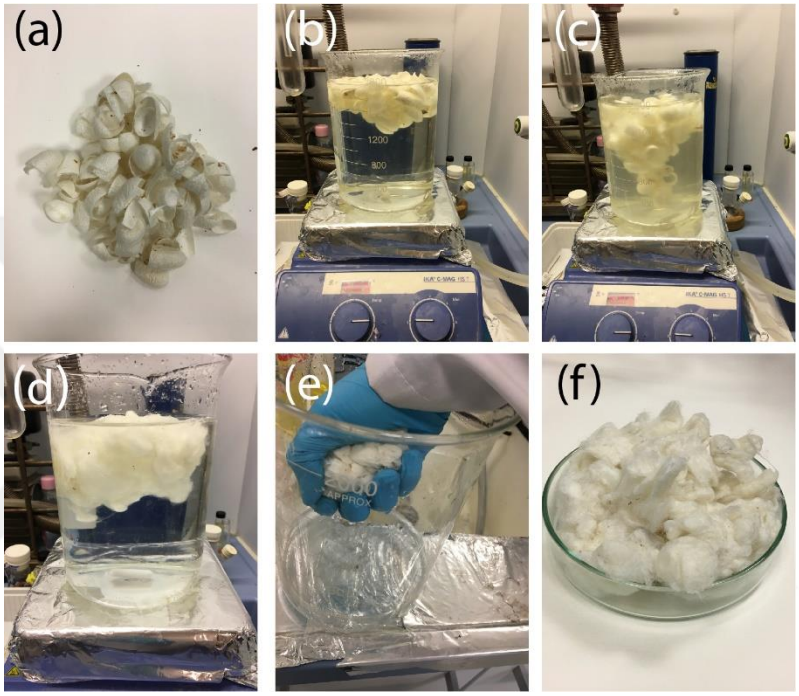

Figure 3.2 (a) Cut silk cocoons. **(b)** Boiling cocoons in 0.02 M aqueous Na2CO3 solution and **(c)** stirring using a magnetic stirrer. **(d)** Rinsing degummed SF in deionized water and **(e)** squeezing it. **(f)** Degummed SF left in room temperature to dry.

The next step is dissolving the dried SF (Figure 3.3-a) in aqueous 9.3 M lithium bromide (LiBr) solution to break the hydrogen bonds and make SF transparent. The added amount of LiBr is calculated using Formula 3.1.

$$(86{,}65\ \text{g/mol}) \times (9{,}3\ \text{mol/L}) \times (1\ \text{L}/1000\ \text{mL}) \times (4X) = \text{m gr LiBr} \qquad (3.1)$$

where *X* is the amount of degummed SF and *m* is the amount of LiBr. After SF is added to the LiBr solution (Figure 3.3-b), the mixture is placed in an oven at 60 °C for 4 hours (Figure 3.3-c). The viscous mixture is injected into a dialysis cassette to separate LiBr and other contaminants. The dialysis cassette is placed inside the water and stirred. The cassette lets the water move in inside while LiBr and other contaminants go out (Figure 3.3-d).

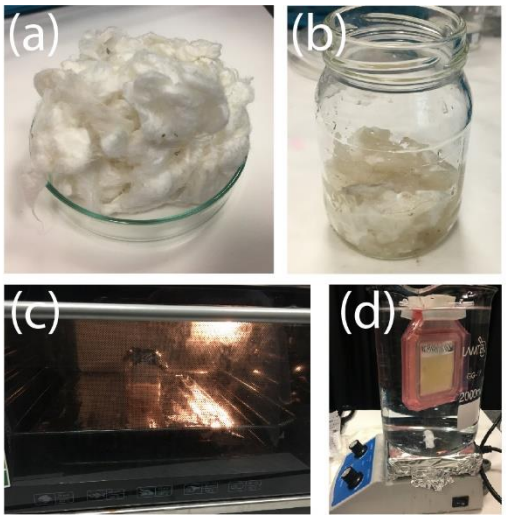

Figure 3.3 (a) Dried SF. **(b)** Mixing LiBr solution with SF and **(c)** inserting the mixture into the oven. **(d)** The dialysis procedure of viscous mixture inside distilled water.

The dialysis procedure lasts for 2 days by changing the distilled water 5 times at time intervals (Figure 3.4-a). Next, the SF solution taken from the cassette is centrifuged at -2°C for 20 minutes with 9000 rpm twice [20]. Finally, we obtain a 7-9 wt% aqueous SF solution.

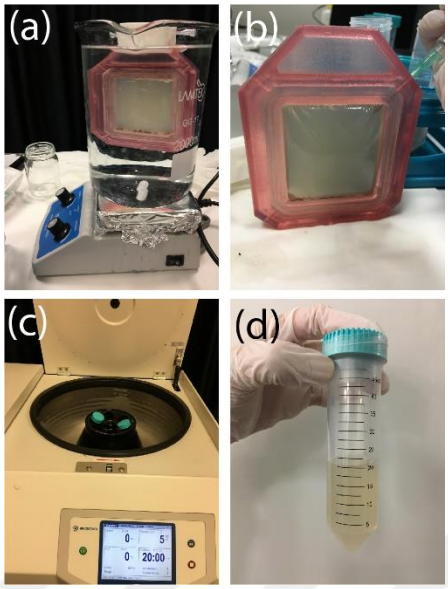

Figure 3.4 (a) Dialysis of SF after 2 days. **(b)** Removing the aqueous SF solution from the cassette. **(c)** The centrifuge of the aqueous SF solution. **(d)** Transparent aqueous SF solution.

SF is a beneficial material being biocompatible, biodegradable, and mechanically robust [21]. Moreover, it is optically transparent [22]. Figure 3.5 shows the absorbance spectrum of a 500 µm-thick SF film dried on a glass slide while inset is the photograph of a transparent SF film.

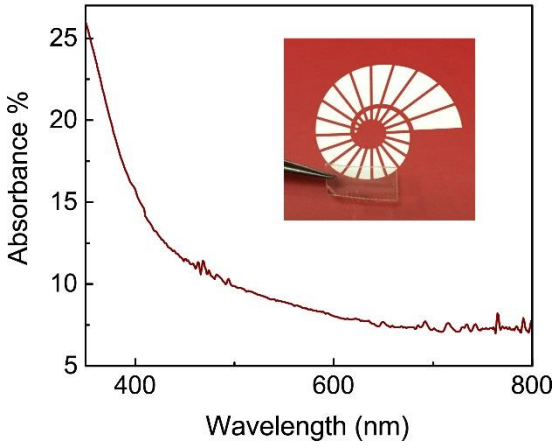

Figure 3.5 Absorption spectrum of an SF film (Inset: Photograph of an SF film).

SF consists of the beta-sheet crystallite domain and amorphous domain (Figure 3.6). Since the SF solution is aqueous, it is easy to process. When the water evaporates, polymer chains gather easily by hydrogen bonding between N-H and C=O of amide groups.

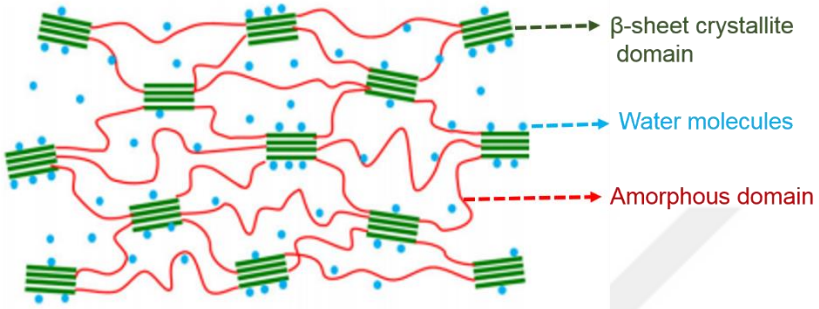

Figure 3.6 Aqueous SF solution structure [23].

3.1.2 Fluorescent Protein Expression and Purification

Fluorescent proteins gained significant attention in biomedical technologies as they illuminate and track the cells and tissues [24, 25]. To produce fluorescent proteins, transformed Escherichia coli (E. coli) cells are used. Firstly, GST-tag containing vector is converted into E. coli cells that are grown on plates. Enhanced Green Fluorescent Protein (eGFP) (30 kDa) and GST tag (26 kDa) are linked to the N terminal of the protein eGFP-GST vector. After a bacterial colony is chosen, large scale growth is initiated. Proteins are expression is induced using 1 mM isopropyl β-d-1-thiogalactopyranoside. After protein expression bacteria cells are pelleted with centrifugal force, and cells are lysed using lysozyme enzyme and washed using GST Wash Buffer (1X PBS (phosphate-buffered saline), 0.25 M KCl, freshly supplied with 25 µg/mL LPC, 17.4 µg/mL PMSF, and 10 µg/mL Aprotinin). After freezing-thawing-sonicating the cells, superflow glutathione agarose beads are utilized for protein purification. Elution buffer (50 mM Tris pH 8.0, 10 mM Glutathione, freshly supplied with 10 mM DTT, 25 µg/mL LPC) is added to the proteins and eluted with centrifugal filters. Proteins are concentrated on the same filters. Last, eGFP is concentrated 1X PBS (phosphate-buffered saline) is passed through the filter until eGFP is concentrated

down to 250-300 µL. Then fluorescent proteins are desalted with dialysis membranes and 7.96 mg/mL eGFP solution is obtained (Figure 3.7) [26].

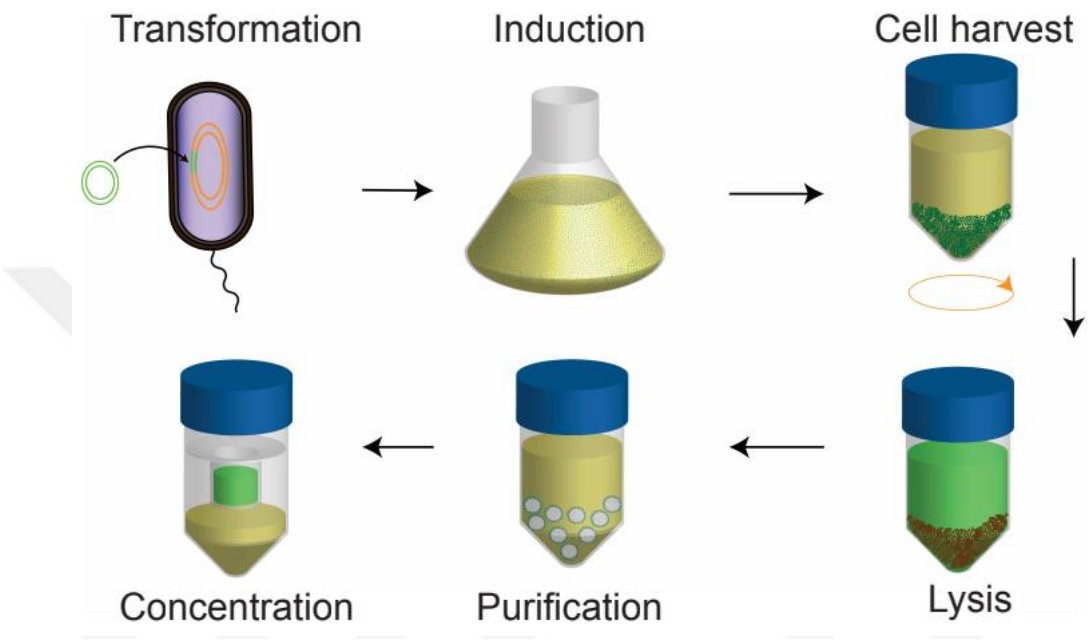

Figure 3.7 eGFP expression and purification [27].

3.2 Optical Set-up

To analyze the emission properties of the samples, we used 10 Hz Quanta-Ray INDI pulsed neodymium-doped yttrium aluminum garnet (Nd: YAG) laser with a pulse width of 5-8 ns [28]. To tune the pump wavelength, a BasiScan optical parametric oscillator (OPO) (SpectraPhysics) is positioned in front of the laser [29] (Figure 3.8). OPO consist of a nonlinear beta barium borate (BBO) crystal that divides the incoming wave into Idler (709.5-2550 nm) and signal (405-709.4 nm) waves. The output wavelength is adjusted changing the BBO orientation.

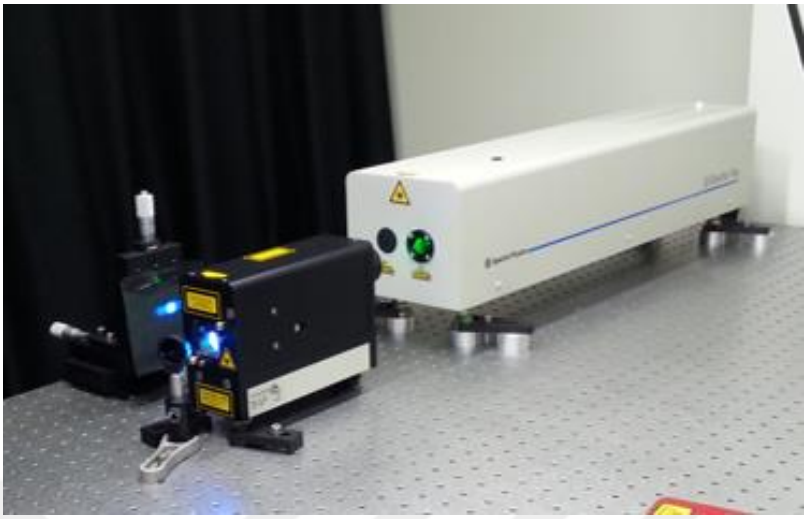

Figure 3.8 Nd: YAG laser (right) and OPO (left).

To examine the emission properties of our samples, we coupled the emitted waves into an Andor Shamrock 500i Spectrograph mounted with Andor Newton Cooled Spectroscopy Camera with 0.03 nm resolution (Figure 3.9-a). The input light passes from the slit through concave lenses and arrives at the gratings. The grating diffracts the light with different angles in terms of wavelength. Before the light arrives at the camera, it is collected by a concave lens as shown in Figure 3.9-b.

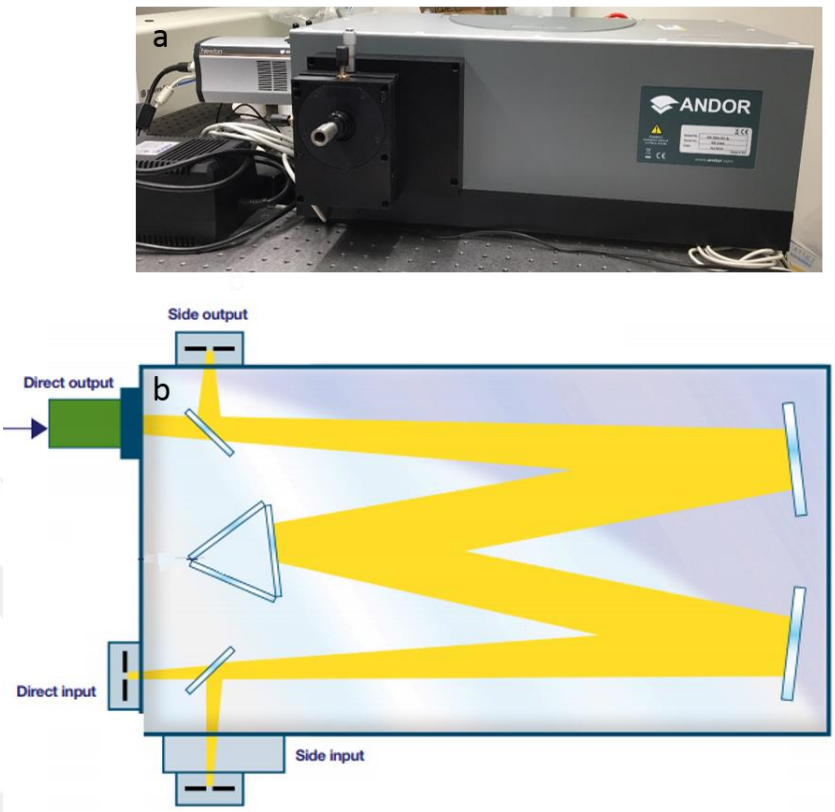

Figure 3.9 (a) Spectrograph and **(b)** schematic view of its design used in laser experiments [30].

Chapter 4

SELF-ASSEMBLED WHISPERING GALLERY MODE LASERS

The coffee stain effect is a beneficial method to produce WGM resonators because, in the coffee stain effect, droplets of colloidal solutions transform into perfect circular structures. The light coupled into circular structures has round trips along the perimeter of the circle and lase when it interferes with itself constructively. In this chapter, we analyze the effect of solution concentration and surface properties (e.g. surface area, hydrophobicity) and temperature, we obtain disks and spheroids and use them as optical cavities in biolasers.

4.1 Self-assembled Spheroid Whispering Gallery Mode Lasers

Reproduced (adapted) from Ref. [31] with permission from the Royal Society of Chemistry.

In this section, the coffee stain effect that forms 2D structures is used to generate 3D structures that we nominated 3D coffee stains. At first, we showed the transformation of a coffee ring into a 3D coffee stain. Then, we made a parametric study based on surface contact angle and solution concentration. Finally, to increase the surface quality of 3D coffee stains, adapting from the pendant droplet approach we decreased the contact area of the surface with the droplet, enhanced surface quality of stains to be used as biolasers.

4.1.1 3D Coffee Stain Formation

To investigate the 3D coffee stain formation, an aqueous photoluminescent SF solution modified with eGFP is placed on a superhydrophobic surface, with a water contact angle (WCA) greater than 150° [32]. Water tries to minimize its contact on hydrophobic surfaces. When the surface is roughened by hydrophobic nano and microstructures, it transforms into a superhydrophobic surface. The droplet pinning area to the substrate decreases excessively. Figure 4.1 shows the superhydrophobic polydimethylsiloxane-urea (SHPSU) surface used to

produce 3D coffee stain. The surface is produced by the introduction of silica particles (1 to 10 μm in size) which are randomly distributed on the polymer surface.

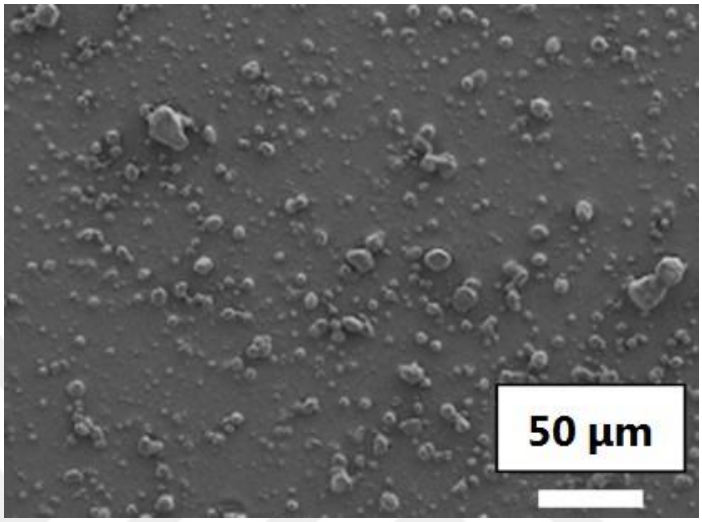

Figure 4.1 Superhydrophobic SHPSU surface.

While the same protein solution generates a 2D ring on a hydrophilic poly(methyl methacrylate) (PMMA) surface (Figure 4.2-a), a superhydrophobic surface allows the formation of a 3D spherical structure (Figure 4.2-b). The process from liquid droplet to 3D solid form can be divided into two main stages. As shown in Figure 4.2-b, in the first stage (0 - 16 min) the droplet volume becomes smaller due to evaporation. The spherical droplets exhibit d-square law behavior

$$(D^2/{D_0}^2 = 1 - kt/{D_0}^2) \tag{4.1}$$

where D is the droplet diameter as a function of time during the evaporation process, D_0 is the initial droplet diameter, k is the evaporation rate and t is the time (Figure 4.1-c). This square law behavior means that the solvent and air interface dominates the droplet

vaporization [33]. The diameter of the droplet decreases (k = 0.037 mm^2/s) to a steady-state value and then stays approximately the same (Figure 4.2-c). Besides, it is important to note that the pinned contact area both in 2D and 3D stain formation (Figure 4.2-a and b, respectively.) stays constant during evaporation. To keep the contact area fixed, the particles in the liquid flow in a radial motion towards the edges as in the 2D coffee stain formation [4]. As a result, the formation of 3D coffee stain proceeds with the construction of the 2D ring at the three-phase contact line, which can be considered as the first stage.

While the evaporation continues, the solvent permeation flux is higher on the surface of the droplet than its interior, and the flow due to the radial migration piles up the colloidal particles on the edges of the 2D coffee stain. The continued stacking of the particles initiates the formation of droplet skin on the initial coffee stain ring. Furthermore, since the surface energy of water (72.6 mN/mm) is much higher than that of SF (43-52 mN/mm) [34], skin formation also leads to a substantial reduction in the overall surface energy of the system and thus, it is thermodynamically favorable. The formation of the 3D skin becomes completed on top of the 2D ring at the end of the first stage.

In the second stage (18 - 26 min) the radius of the skin does not significantly change (Figure 4.2-b) while evaporation continues. This is due to the formation of a water vapor permeable, semi-crystalline and robust SF skin on the outer layer of the droplet.

At this point, the droplet has a fairly dense solid-air interface, while the inside is filled with liquid. As the evaporation continues a bubble nucleates in the 3D skin (Figure 4.2-b), which is more clearly observable for a transparent SF droplet (Figure 4.2-d). The volume of the SF solution decreases as the solvent permeates through the skin, which results in the expansion of the bubble inside the droplet and reinforcement of the 3D skin. The 3D spheroid surfaces remain fairly smooth during the evaporation process. At the end of the evaporation, a 3D coffee stain is formed.

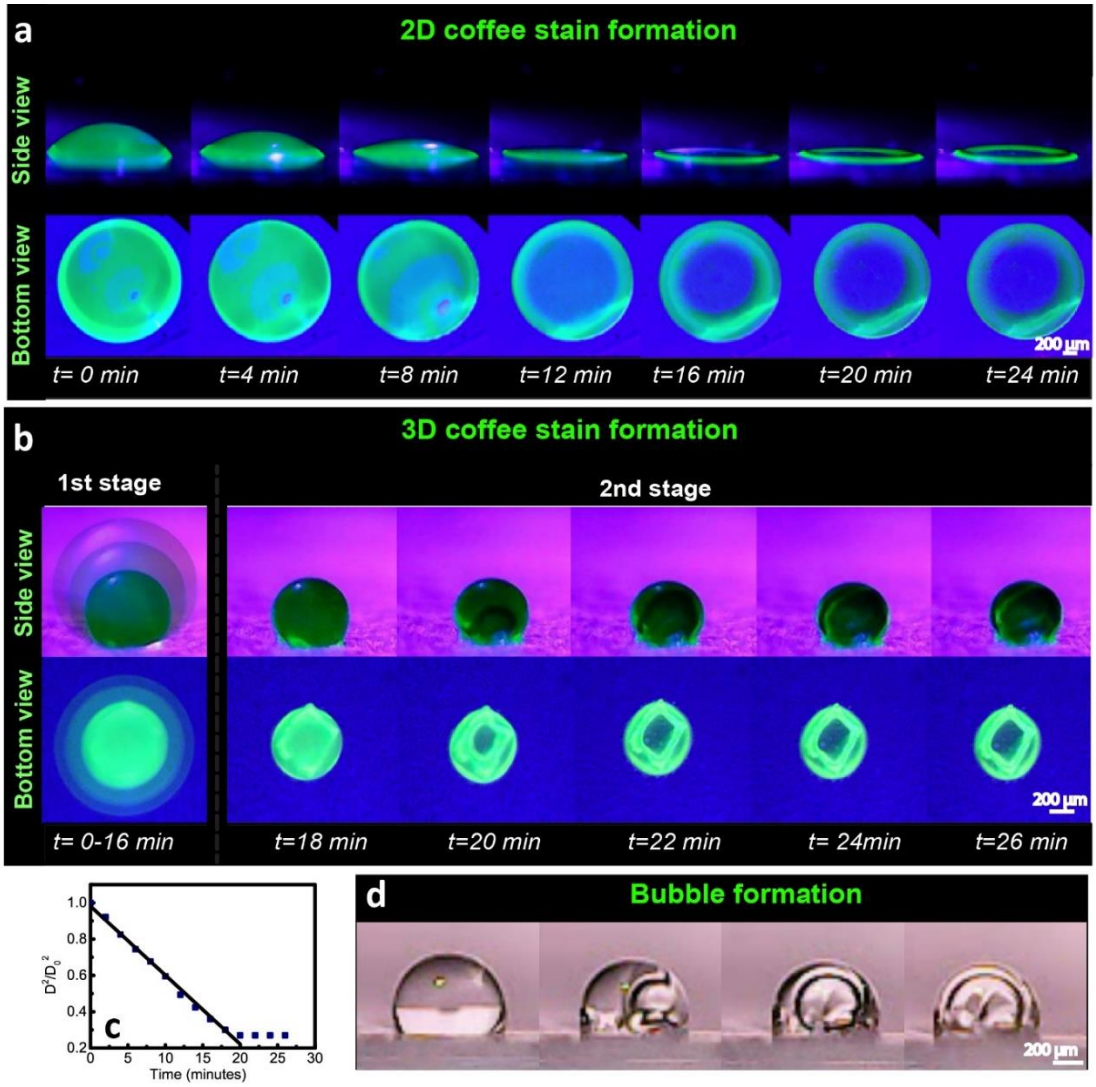

Figure 4.2 Formation of **(a)** 2D and **(b)** 3D coffee stains from a colloidal, aqueous eGFP modified SF droplet placed on a hydrophilic and a superhydrophobic surface, respectively. **(c)** The change in the droplet diameter (D^2/D_0^2) on the superhydrophobic surface as a function of time. **(d)** Demonstration of bubble formation using transparent SF solution on the superhydrophobic surface.

The structure of a 3D coffee stain was analyzed using confocal microscopy (Figure 4.3-a). The 3D coffee stain has sub-millimeter dimensions with a height of 660 µm (in the z-direction) and a maximum outer radius (r_{out}) of 477 µm (in the xy plane) (Figure 4.3-b and c). Starting from the top (z=660 µm) while we image the sphere downwards (-$\hat{z}$ direction),

we observe the first cavity at the z=465 µm plane. At this point, the vertical thickness of the upper wall is 215 µm and the lateral wall thickness in the xy plane (t) is 400 µm, which is equal to the outer radius. Afterward, the internal radius (r_{in}) of the sphere starts to increase and it reaches a value of 310 µm (at z=330 µm). At the same time, the lateral wall thickness decreases to 170 µm. Thus, the coffee stain effect can generate well-organized and robust 3D structures on a superhydrophobic surface.

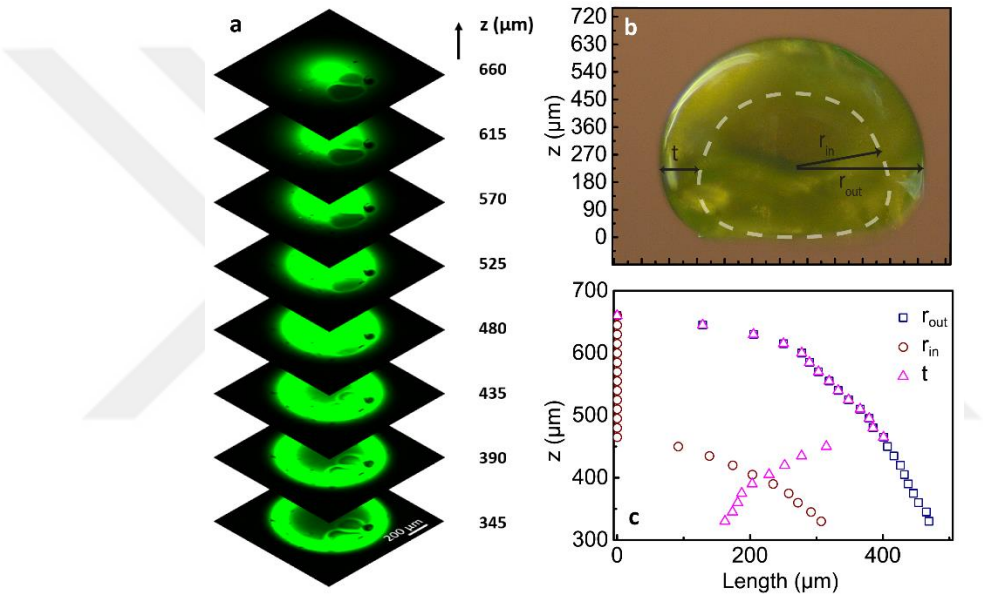

Figure 4.3 (a) Confocal z-stack images of eGFP modified SF 3D coffee stain formed on the superhydrophobic surface, **(b)** the side view and schematic description of the 3D stain with outer (r_{out}) and inner (r_{in}) radius, and wall thickness (t) in the xy plane, and **(c)** their values in z-direction.

4.1.2 Influence of Surface Hydrophobicity and Solution Concentration on the Topography of the 3D Coffee Stains

Our studies indicate that the contact angle (CA) of the substrate is critical for the formation of 2D or 3D coffee stains. To explore the effect of the substrate surface, we kept the concentration of SF constant at ca. 7-9% by weight and utilized four different substrates

PMMA (64°), silicon rubber (PDMS) (94°), Teflon tape (PTFE) (123°) and SHPSU (165°), where WCA are provided in parenthesis. Images provided in Figure 4.4-a show the droplet structures on initial (top images), mid (middle images), and final (bottom images) stages of the protein solution evaporation on these surfaces. Droplets on PMMA and PDMS surfaces resulted in coffee stains with flat domes, similar to conventional 2D coffee stains. On the other hand, a highly hydrophobic PTFE surface resulted in a collapsed dome indicating a transition from 2D to 3D coffee stain. As the substrate surface became superhydrophobic, the protein deposition on the pinned base increased leading to skin formation and a stable 3D dome (Figure 4.4-b). For all samples, the droplet heights decreased with time until reaching a stable level. Only the droplet on the superhydrophobic surface exhibited an earlier plateau value for dome height. Moreover, there is a correlation between the initial CA of the solution and the final CA of the solid structure. As the hydrophobicity of the surface increases, the final value of the contact angle increases as well (Figure 4.4-c). While CA of the droplets on all surfaces continues their decrease until complete evaporation, the superhydrophobic surface, which starts with a CA of 145°, reaches to a fairly high final CA of 95°. These results demonstrate the critical effect of surface hydrophobicity on the formation of 3D coffee stain.

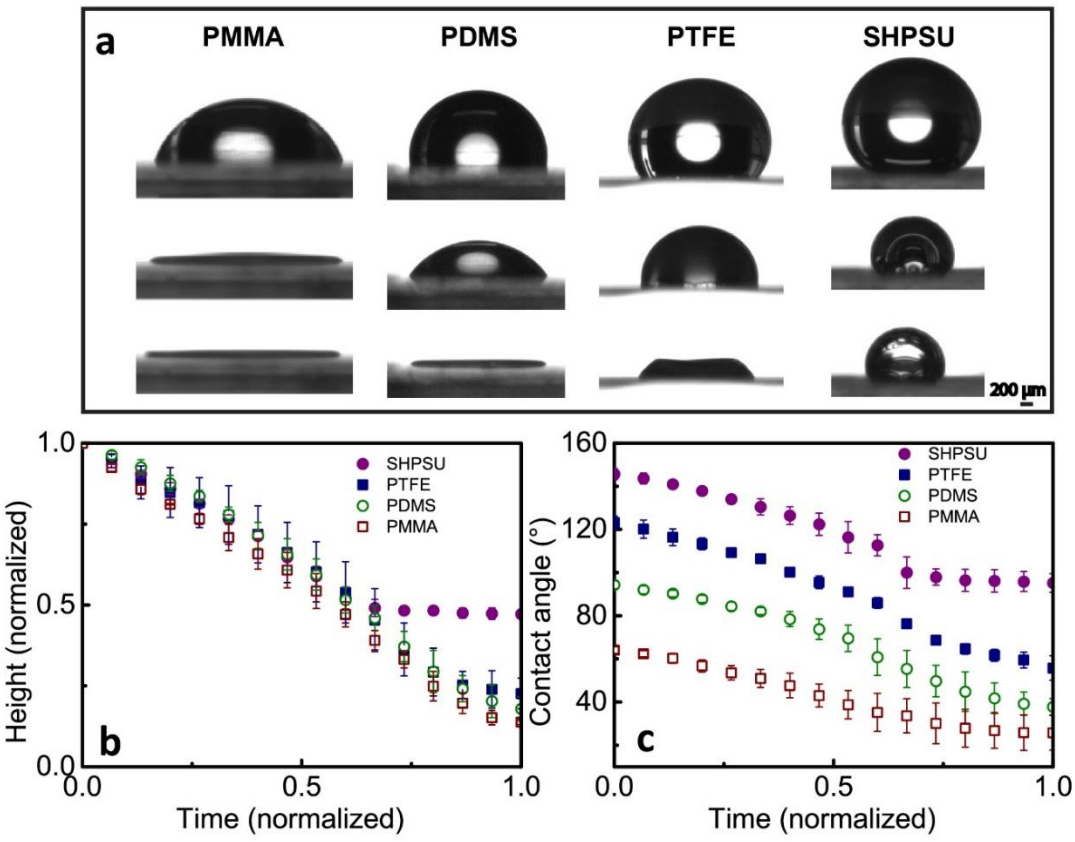

Figure 4.4 (a) Images of aqueous SF droplets on PMMA, PDMS, PTFE, and SHPSU at the initial (top images), mid (middle images), and final (bottom images) stages of evaporation, and time-dependent **(b)** droplet height, and (**c)** contact angle.

The effect of solution concentration on the formation and the structure of the 3D coffee stain was also investigated. For this purpose, droplets were deposited on a superhydrophobic surface using SF solutions with concentrations of 1.0, 2.0, 4.0 and 8.0 wt%. As expected, the initial CA is highest for the solution with the lowest concentration, which approaches to the water contact angle (without any protein). On the other hand, the final CA of 3D stains gradually falls, while the concentration decreases because lower concentration leads to a weak skin formation that starts to perturb the spherical shape of the dome and may even collapse (see 1% and 2% solutions in Figure 4.5-a). As the concentration increases, a self-standing and spherical 3D coffee stain is formed. Also, the time to reach plateau values decreases with increasing concentration as expected (Figure 4.5b and c).

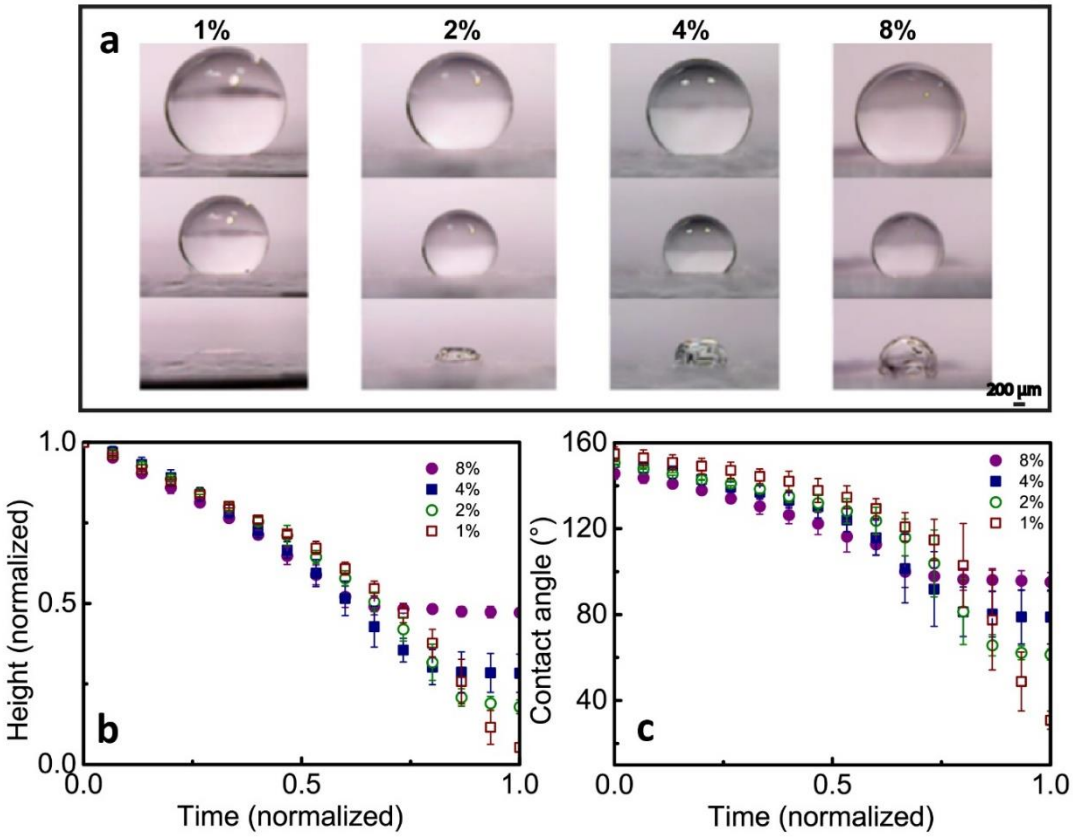

Figure 4.5 (a) Images of aqueous SF droplets with different concentrations on SHPSU surfaces at the initial (top images), mid (middle images) and final (bottom images) stages of evaporation, and time-dependent **(b)** droplet height, and **(c)** contact angle.

4.1.3 3D Coffee Stains for Lasers

Spherical 3D coffee stains with a smooth surface can facilitate the light oscillation in the solid-air boundary that can generate a WGM resonator. Even though the superhydrophobic surfaces were useful to generate 3D stains, the quality of the surfaces obtained were not at a sufficient level to utilize it as an optical cavity. As a further improvement in the structure and the surface quality of 3D coffee stains, we adapted a pendant-drop approach. A blunt stainless steel needle was used to suspend a pendant droplet of aqueous eGFP blended SF solution.

The spherical shape of the pendant droplet was maintained throughout the evaporation process due to a very small contact area with the needle tip. Although a perfectly spherical droplet is expected due to the minimization of surface energy, as shown in Figure 4.6, a slightly elongated pendant droplet is formed as a result of the gravitational force. As shown in the superimposed images provided in Figure 4.6-a, until the outer skin is formed, the droplet diameter shows a fairly constant rate of decrease with a slope of 0.036 mm^2/s (Figure 4.6-b), which is almost identical to that of the sessile droplet. As the evaporation proceeds, the skin formed adheres to the tip of the needle and an air bubble is formed similar to those observed on superhydrophobic surfaces. The shape and the size of the droplet do not change after the skin formation and the air bubble keeps expanding until complete evaporation of water, eventually leading to the formation of a spherical 3D coffee stain with enhanced surface quality as shown in Figure 4.6-c.

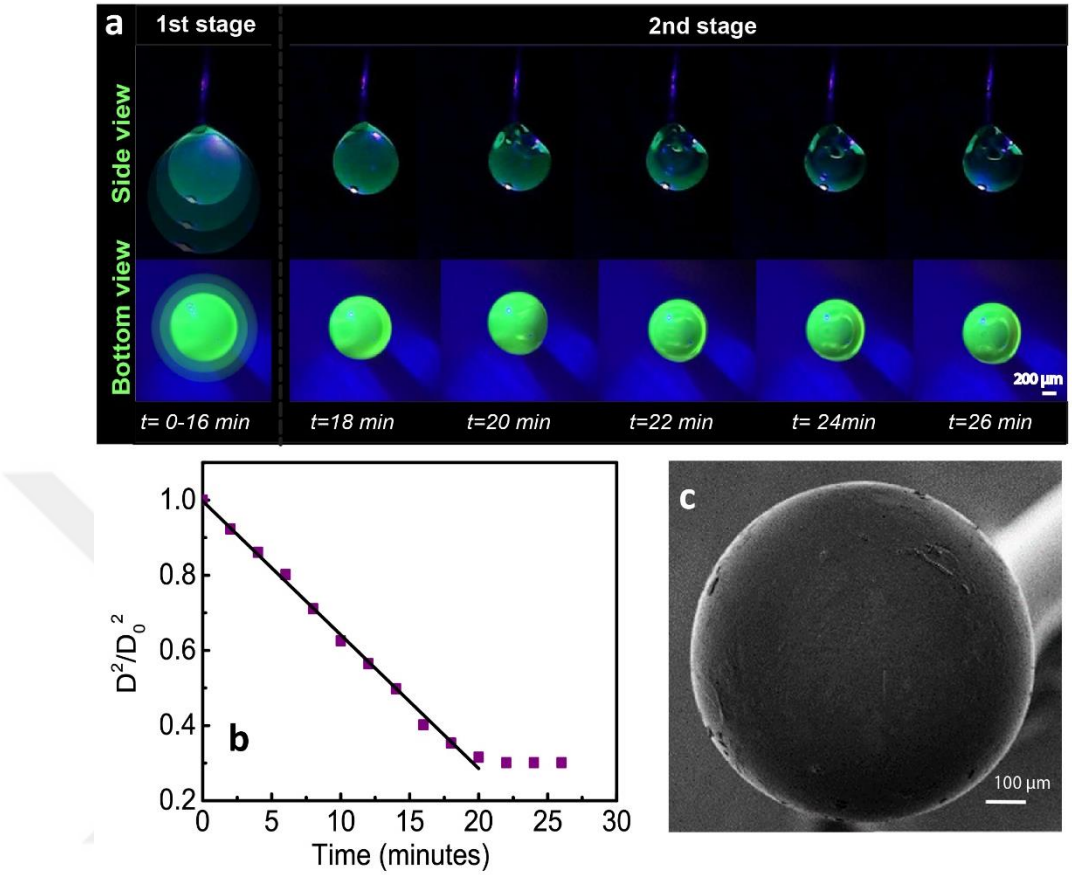

Figure 4.6 (a) 3D coffee stain formation from aqueous eGFP modified SF pendant droplet. (**b)** Change in the pendant droplet diameter (D^2/D_0^2) as a function of time. (**c)** SEM image of 3D coffee stain (bottom view).

To generate an all-protein laser, initially, we explored the amplified spontaneous emission (ASE) of eGFP in transparent SF protein. A thin film of SF containing eGFP was utilized for ASE experiments via the variable stripe length (VSL) method. Using a cylindrical lens (Figure 4.7-a), a focused narrow line of a laser beam at 482 nm, which overlaps with the strong absorption band of the eGFP, excited a stripe on the slide, which functioned as a one-dimensional optical amplifier. While spontaneous emission was generated in random directions as the pump flux was increased, emitted photons were amplified through the stripe due to population inversion and were collected. As shown in Figure 4.7-b, the spectral narrowing at 521 nm demonstrates the amplified spontaneous emission (Figure 4.6-c). This

result shows that fluorescent protein in an SF matrix has the potential to generate laser emission in a cavity structure.

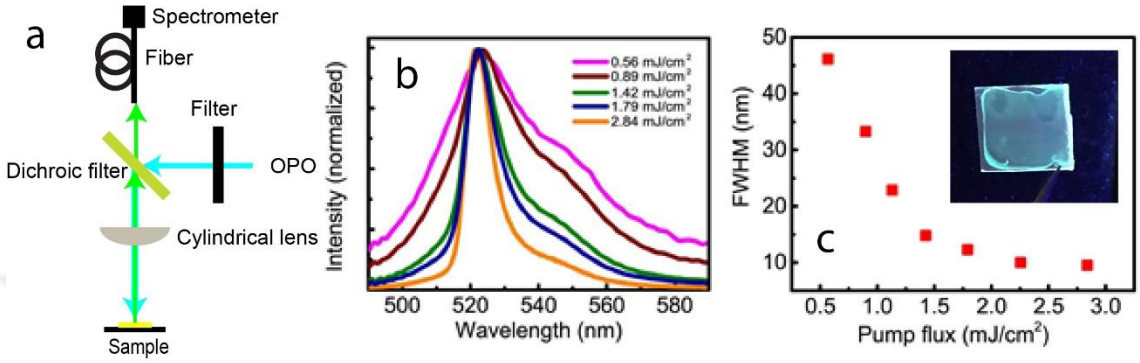

Figure 4.7 (a) Schematic of the optical set-up used in ASE experiments. **(b)** ASE spectra of spin-coated eGFP modified SF protein film under various pump levels. **(c)** The full width at half maximum (FWHM) of ASE as a function of pump flux. Inset shows the eGFP doped SF spin-coated glass slide.

Spherical 3D coffee stains obtained by using pendant droplets advantageously increase the surface quality for lasing (Figure 4.8-a). To generate laser emission, Quanta-Ray INDI pulsed Nd: YAG laser with a BasiScan OPO (SpectraPhysics) is used. The pump with a repetition rate of 10 Hz is passed through an optical density (OD) filter where the laser energy is adjusted. Then, the laser arrives on the sample via a 10X microscope objective. The emitted light from the sample is collected by a fiber placed to the side of the sample (i.e., orthogonal to the direction of the pump light) and reached to the spectrometer (Torus Concave Grating Spectrometer, Ocean Optics) as shown in Figure 4.8-b. eGFP containing SF spheroid was pumped with 5 ns OPO pulses ranging from 0.3 μJ to 234.7 μJ at 482 nm and a laser threshold behavior was observed at 37.15 μJ, where the slope efficiency increased 7.3 times in comparison with the subthreshold condition (Figure 4.8-c and d). Laser emission was further confirmed with spectral narrowing above the threshold. Even though in the subthreshold regime the peak at 521 nm dominates the emission due to ASE, in the suprathreshold region a new and narrowing peak due laser emission is observed at 547 nm, which drastically

increases above the threshold (Figure 4.8-d). Thus, the threshold and spectral behavior prove the laser emission by the 3D stain. Due to the limited resolution of the detector (≈ 1 nm), the longitudinal and transverse modes were not distinguishable for such a millimeter-scale sphere. The 3D spheres obtained using aqueous SF solutions, which are biodegradable, biocompatible, and transparent have unique properties for cavity formation. Moreover, the biologically produced fluorescent protein of eGFP presents an important natural biomolecule as a laser gain medium in SF [8]. Thus, the spherical 3D coffee stains obtained using pendant droplets of eGFP modified SF solutions enabled the construction of all-protein lasers.

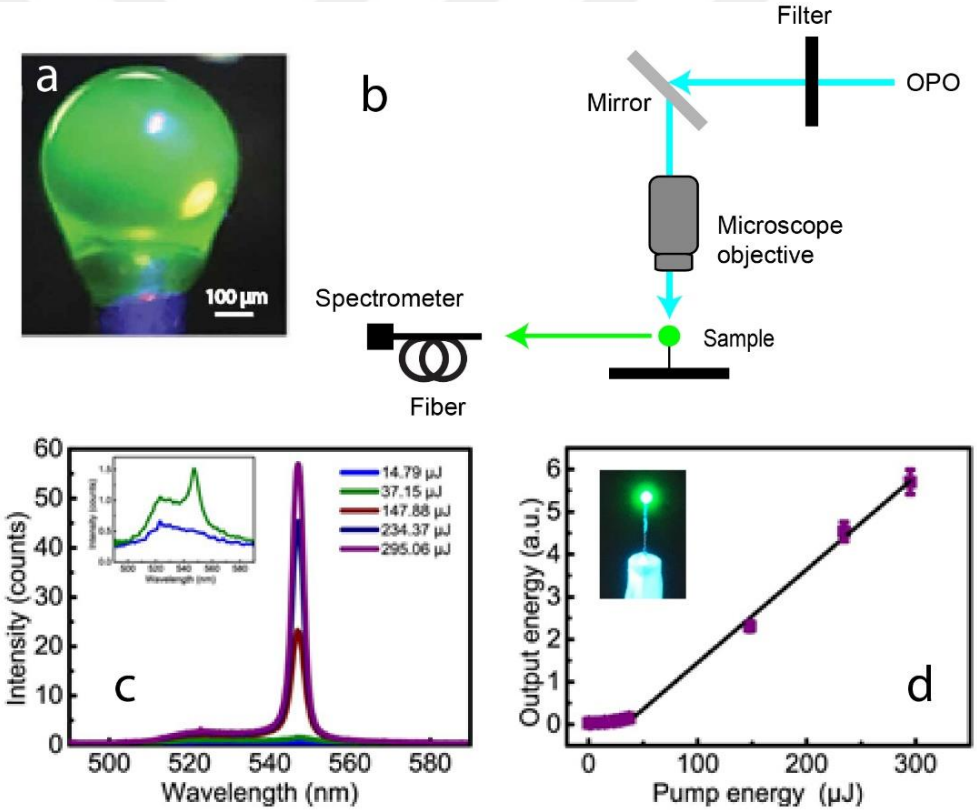

Figure 4.8 (a) Image of the 3D protein stain under blue light. **(b)** The optical set-up used in laser experiments. **(c)** Emission spectra of protein laser at different pump levels. Inset: Zoomed emission spectrum at 14.79 and 37.15 µJ. **(d)** The output energy of the protein laser as a function of pump energy. Inset**:** Image of 3D stain while lasing.

4.2 Self-assembled Disk Whispering Gallery Mode Lasers

Reprinted (adapted) with permission from I. B. Dogru, R. Melikov, and S. Nizamoglu, "Biomaterial Disk Lasers by Suppressing the Coffee Ring Effect," ACS Biomaterials Science & Engineering, vol. 4, no. 12, pp. 4385-4390, 2018. *Copyright 2018 American Chemistry Society.*

Here, the effect of heat in coffee ring phenomena is analyzed. Heating the droplet facilitates the evaporation and prevents the particle flow to the droplet edges. The particles gather at the air-liquid interface [35]. Since the surface descending rate is faster than particle diffusion, the coffee stain effect is suppressed and a uniform film is obtained. We analyze the effect of solution concentration and temperature in the stain formation. We utilize this method to make disk biolasers that are flexible and physically transient [36]. Moreover, we made a mode analysis of disks in terms of size.

4.2.1 Suppressed Coffee Stain Formation

Using transparent and biocompatible biopolymers of SF and PVP [37, 38] as host materials to form the disks, we doped the biopolymers with the synthetic dyes rhodamine B (RhB) and rhodamine 6G (R6G) to generate gain media. To fabricate the microresonators, we heated the droplets on a polydimethylsiloxane (PDMS) substrate in an aluminum foil cap with a standard incandescent lamp (42 W, OSRAM CLASSIC 230 V), as illustrated in Figure 4.9-a. We used the lamp because it can produce heat and light simultaneously, which enables both the adjustment of the environmental temperature within the necessary range of 45–90°C and the visualization of the processes under illumination. We placed the disks inside the aluminum cap when the temperature reached 45°C and maintained a distance of 1.5 cm between the lamp and the droplets. Figure 4.9-b depicts the disk formation of the droplets. After placing the droplets containing the SF and RhB mixture onto the surface (t = 0), we observed a contact angle of 94.4 ± 1.8 and the beginning of liquid evaporation. As a characteristic of the coffee ring effect, coffee ring formation commenced at the pinned edges, and the particles moved toward the pinned edges due to the capillary flow (t = 1 min). Next,

the polymers began to coagulate due to evaporation, which started from the edge and continued toward the center of the droplets (t = 1–3 min). Once the droplets had completely evaporated, a disk made of biomaterial and dye formed (t = 4 min). When we used a heater or oven to heat the droplets, we obtained the same results due to an increase in water evaporation rate and suppression of the coffee ring effect. Numerous disks can be produced by using that method, and Figure 4.9-c presents the RhB- and R6G-doped SF disks. The SEM image of the SF disks shows that the surface was highly smooth (Figure 4.9-d), which corroborated the surface profile measured with an atomic force microscope (AFM) as well (Figure 4.10-a and b).

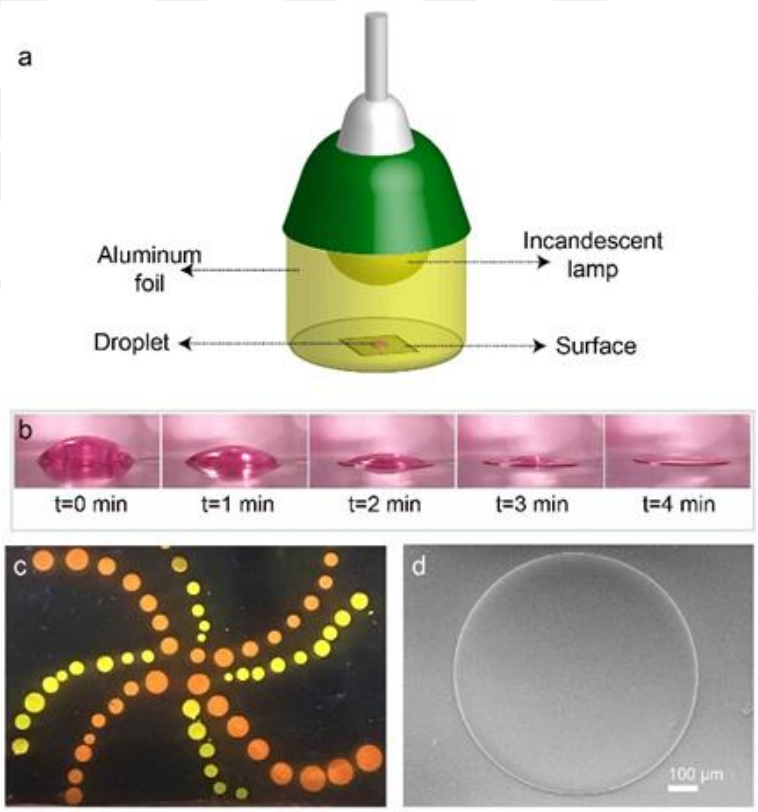

Figure 4.9 (a) Schematic of the setup for disk production, which consists of an incandescent lamp covered by aluminum foil. When placed on a hydrophobic surface inside the aluminum cap, the droplets form a disk after evaporation. **(b)** The transformation of the RhB–SF solution from a droplet to a disk structure on PDMS as a function of time. **(c)** Arrays of RhB- and R6G-doped SF disks on PDMS under ultraviolet light. **(d)** The SEM image of an SF disk.

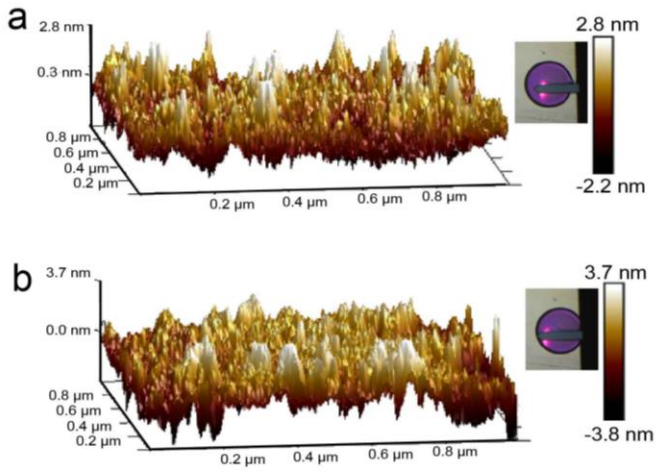

Figure 4.10 The AFM image of an SF disk taken from (a) the center and (b) close to the edge.

We further analyzed the disk structure, as shown in Figure 4.9-d. The AFM measurement taken from the side of the disk revealed that the disk had a thickness of 10 µm, and the sidewall presented a smooth convex profile that allowed light oscillation via TIR (Figure 4.11-a). We also analyzed disk samples by using attenuated total reflectance (ATR) Fourier-transform infrared spectroscopy (FTIR) to understand the molecular structure of the SF in the disk (Figure 4.11-b). In a control group, spin coating the SF resulted in an amorphous structure with an amide I peak at approximately 1,641 cm^{-1}, whereas the methanol treatment of the amorphous silk film shifted the peak to approximately 1,622 cm^{-1} due to β-sheet crystal formation [39]. The self-assembled disk thus showed an amorphous silk structure similar to the spin-coated films.

Next, we investigated the effect of temperature and biomaterial concentration on disk formation (Figure 4.11-c). We observed conventional coffee rings at a temperature of 26°C. At 45°C, the coagulated polymers on the surface of the droplet filled inside the ring, which generated a disk structure. At 65°C, faster evaporation limited the time for particle deposition, and the surface of the disks became deformed. Accordingly, we determined the appropriate starting temperature for disk formation to be 45°C, at which the solution's concentration also directly affected disk formation. As the concentration decreased from 8%,

at which disk formation could properly occur, the amount of polymer colloid that can fill the inside of the coffee ring decreased which resulted in regular coffee rings.

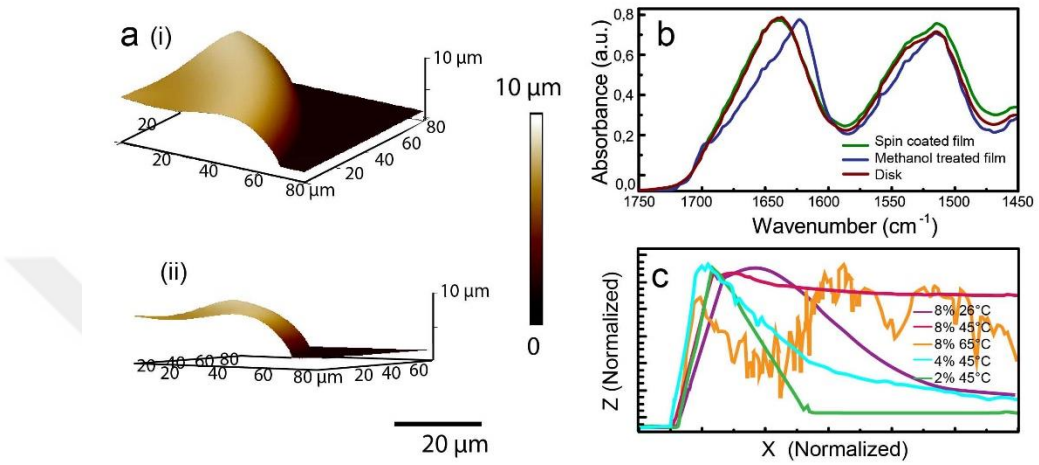

Figure 4.11 (a) AFM images of an SF disk. The parts close to the edges were measured to observe the thickness of the disk. **(b)** ATR–FTIR of spin-coated, methanol-treated silk films and the disk. **(c)** White light interferometric images of coffee ring formed at different temperatures and concentrations. The y-axis, representing the height profile in the z-direction, is normalized with respect to the different fabrication conditions for the maximum height of each disk, whereas the x-axis, representing the position of each height, is normalized with respect to the measured length from the edge of the disks. The legends refer to the concentration of the SF solution and the initial fabrication temperature of the disks.

4.2.2 Whispering Gallery Mode Disk Lasers

We conducted laser experiments with the optical setup shown in Figure 4.12-a. To pump the disks, we used a laser of 10 Hz Nd: YAG with a pulse width of 5–8 ns and adjusted the wavelength to 482 nm by using an optical parametric oscillator. We altered the input laser energy by using OD filters from 1.36 nJ/µm^2 to 43 nJ/µm^2. We collected the emitted light from the disk by using a fiber placed to the side of the sample and measured it by using a spectrometer with a spectral resolution of approximately 1 nm. Figure 4.12-b depicts the

absorption and photoluminescence of RhB inside the SF solution. Since the absorption and emission effectively intersected in the interval from approximately 550 nm to 590 nm, the laser emission was more observable at longer wavelengths on the emission spectrum, at which the absorption had less strength.

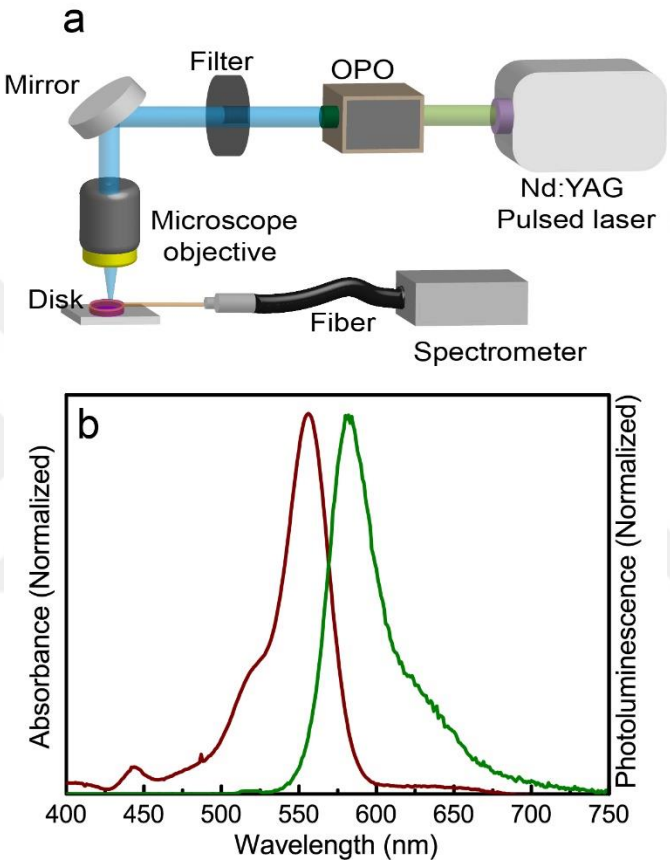

Figure 4.12 (a) Schematic illustration of the optical setup. **(b)** Absorbance and photoluminescence spectrum of RhB in SF solution.

Figure 4.13-a depicts the emission of an RhB-doped SF disk 517.3 μm in diameter on a PDMS layer under different pulse energies. As the pump energy increased, spectrally narrow emission peaks became observable at above 600 nm. We also observed threshold behavior; the integrated output energy increased rapidly above 10.8 nJ/μm^2 (Figure 4.13-b). The inset of Figure 4.13-b presents photographs of a disk excited below and above the lasing threshold pump energy, respectively. Next, to assess the laser emission, we cut the same disk from the circumference and repeated the experiments. Since WGM lasers confine the light inside the

cavity produced by TIR in the periphery, structural discontinuity at the edge prevents the light oscillation inside the cavity by increasing the losses, which halts mode formation and the laser emission. Figure 4.14-a and presents the microscopy images and emission spectra of the disk before and after cutting. The emission of the cut disk thus shows a broad emission profile instead of narrow laser emission peaks, as well as a linear dependence as the pump energy increases instead of threshold behavior (Figure 4.13-b), which indicates that the laser emission occurred via a WGM resonator, not a Fabry–Pérot interferometer.

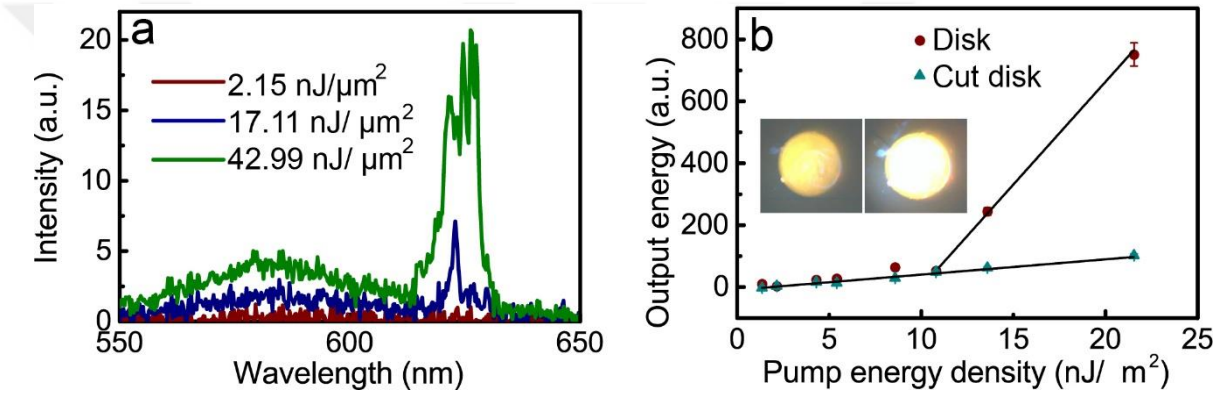

Figure 4.13 (a) Emission spectra of the RhB–SF disk under different pump energy densities and **(b)** its integrated fluorescence intensity in terms of input energy before and after cutting.

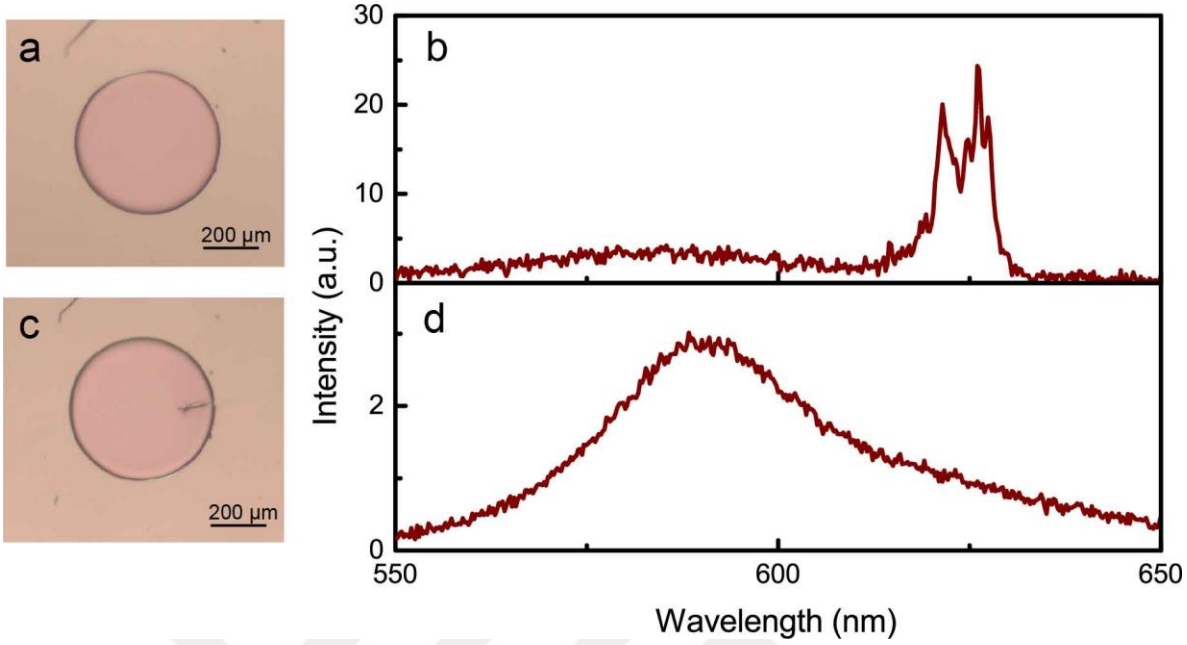

Figure 4.14 (a) A disk on PDMS and **(b)** its emission spectrum. **(c)** The same disk is cut from the edge and **(d)** emission spectrum of the cut disk.

Figure 4.15 depicts the time-dependent laser intensity of an RhB–SF disk. We pumped the disk with an energy density of 43 nJ/µm^2 in 10-Hz pulses for 20 min, and after 12,000 shots, photodegradation of the RhB dye was clearly observable.

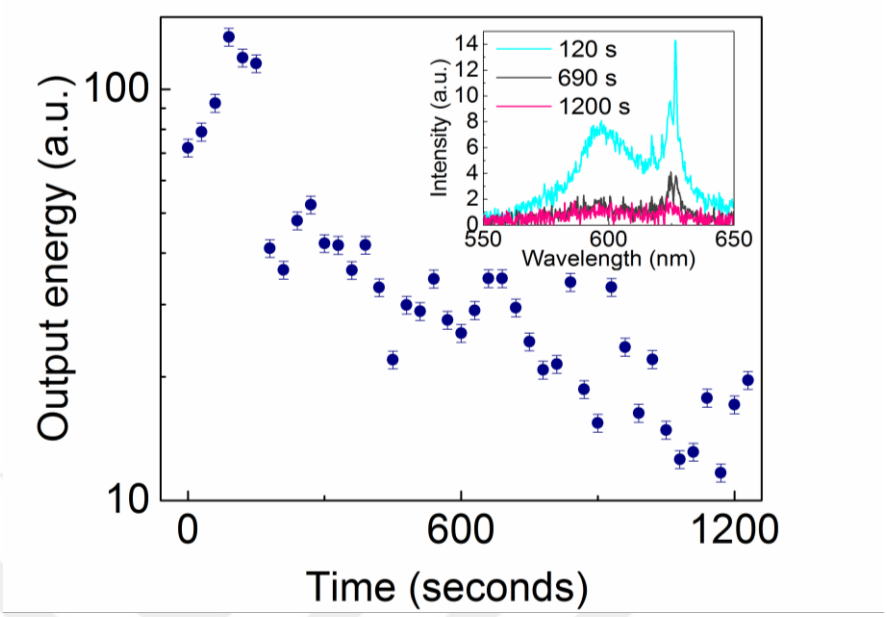

Figure 4.15 Time-dependent lasing intensity of an RhB–SF disk. The disk was pumped with 10-Hz pulses for 20 minutes at an energy level of 43 nJ/μm^2.

4.2.3 Size-Dependent Analysis of Whispering Gallery Mode Disk Lasers

We assessed the lasers by altering the disk size. We fabricated disks with diameters of 267.4 μm, 517.3 μm, and 701.4 μm and investigated their lasing properties (Figure 4.16-a, c, and e). In WGM cavities, the confined wave coherently added to itself when it completed each loop. As the size of the disks increased, the optical path that the light traveled also increased. The relationship between the radius change (ΔR) and wavelength shift ($\Delta\lambda$) is:

$$\Delta\lambda/\lambda = \Delta R/R \tag{4.2}$$

where λ is the laser wavelength, R is the cavity radius [40]. However, this formula does not apply to our samples. We observed ~8.5 nm and ~2.3 nm wavelength shift while the expected shift about 300 nm. This inconsistent result shows that other factors affect the WGM lasing. In coffee stain formation, the particle distribution inside the stains is based on the particle size, and the dye distribution inside the disks may fluctuate [41]. Although we made the

radius change analysis, the height of the disks also differs that results in a gain medium concentration alteration. The relation of light out-coupling power (P_o) and gain spectrum of the dye (g) can be found using the following formulas [42]:

$$P_o \sim [V(R,\lambda) / \lambda^3]\, g(\lambda)\, \beta(R,\lambda) \tag{4.3}$$

where β is the out-coupling efficiency of light and V is the optical mode volume of the cavity. The out-coupling efficiency of light from the cavity to free space can be found using Formula 4.4.

$$\beta = Q_{rad}^{-1} / Q_{total}^{-1} = Q_{rad}^{-1} / [Q_{rad}^{-1} + Q_{abs}^{-1}] \tag{4.4}$$

In Formula 4.4 Q_{rad} stands for the radiative quality factor, Q_{total} is the total quality factor and Q_{abs} is the absorption loss. The light with lower spectral overlap between emission and absorption experienced a higher gain along a longer optical path. For small disks, it was more difficult to confine light with high curvature, since possible defects on the surface could disturb TIR [43]. As a result, outcoupling efficiency increased and blue shifts emerged, which prompted additional losses to lower wavelengths [42]. Therefore, the laser emission shifted toward reddish wavelengths as the diameter of the disks increased. The free spectral range (FSR) decreased as diameter increased at a rate of

$$FSR = \lambda^2 / n\pi D \tag{4.5}$$

in which n is refractive of the cavity and D is the diameter of the cavity. For example, for a disk with a diameter of 267.4 μm, the FSR corresponded to approximately 0.3 nm, which was lower than the spectral resolution of the spectrometer (approximately 1.0 nm). Therefore, we observed a collective emission with a high spectral overlap between the multiple modes. Moreover, as the size of the disks increased, the separation of the observed lasing modes

clearly became closer to each other due to the reduced FSR. The threshold was inversely proportional to the size (Figure 4.16-b, d, and f).

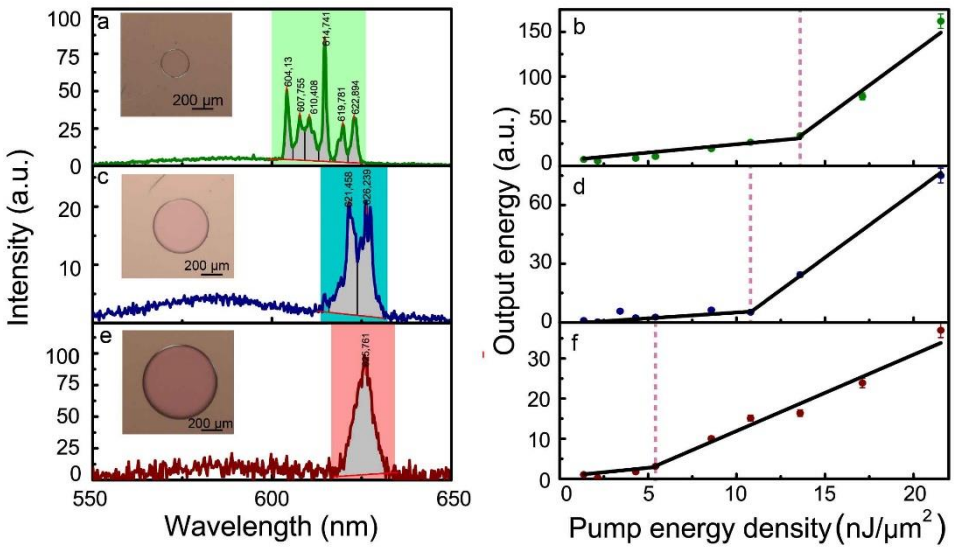

Figure 4.16 RhB-SF disk emission spectra with a diameter of **(a)** 267.4 μm, **(c)** 517.3 μm, **(e)** 701.4 μm, and their corresponding output energy in terms of pump energy, in **(b)**, **(d)** and **(f)**, respectively.

4.2.4 Physically Transient Whispering Gallery Mode Disk Lasers

The biopolymer of the polyvinylpyrrolidone (PVP) was a material generally recognized as safe, according to the U.S. Food and Drug Administration, and widely used in contact lenses, pharmaceutical tablets, and food additives. We fabricated a self-assembled disk by using PVP doped with RhB and analyzed the structure of the PVP disk with a white light interferometer (WLI). Unlike with SF disks, we observed that PVP disks had a slightly convex surface (Figure 4.17-a). In coffee ring formation, because particle size affected the contact line pinning, different polymer sizes, adhesion forces between the particles, and the surface energy of the molecules influenced the deposition of the particles inside the ring [41]. To

reduce the size of the disk, we sprayed the RhB–PVP solution on a PDMS surface and thereby obtained small disks. Figure 4.17-b shows the emission spectrum of a 45.8-µm RhB–PVP disk. At that size, the disk accommodated WGM mode analysis, and we calculated the actual mode number according to the formula

$$\lambda_m = 2\pi rn / m \tag{4.6}$$

in which r is the radius of the disk, n is the refractive index of the PVP cavity (1.53), and m is the mode number. When compared with the calculated theoretical modes, the peak positions agreed with the mode numbers from 336 to 344 (Figure 4.17-c). Moreover, since PVP is a water-soluble biopolymer after we placed the fabricated disk inside an aqueous environment, the disk laser completely dissolved in less than 1 min (Figure 4.18-d).

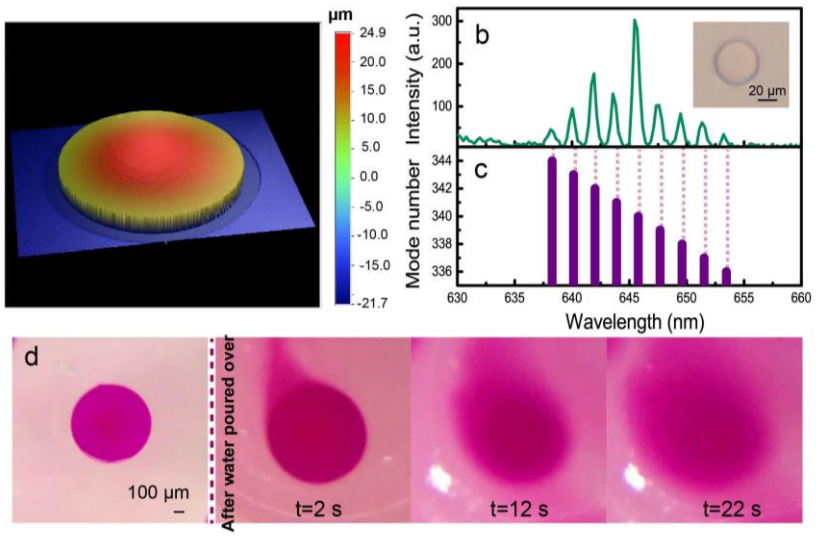

Figure 4.17 (a) The WLI image of a PVP disk. **(b)** The emission spectrum of an RhB–PVP disk and **(c)** calculated mode numbers. **(d)** Left of the dashed line: A RhB–PVP disk on a PDMS surface; right of the dashed line: 20 µL water poured on the disk, which dissolved in 22 s.

We could also detach the disks from the surface and transfer them to other surfaces as well as onto different substrates. Figure 4.18-a displays the image of an RhB–PVP disk 841.9 μm in diameter detached from the PDMS and stuck on tape (MAS® Invisible Tape) rolled on a circular rod with a radius of approximately 1 mm (Figure 4.18-b). The RhB–PVP bent disk also generated a WGM laser as the pump energy increased (Figure 4.18-c).

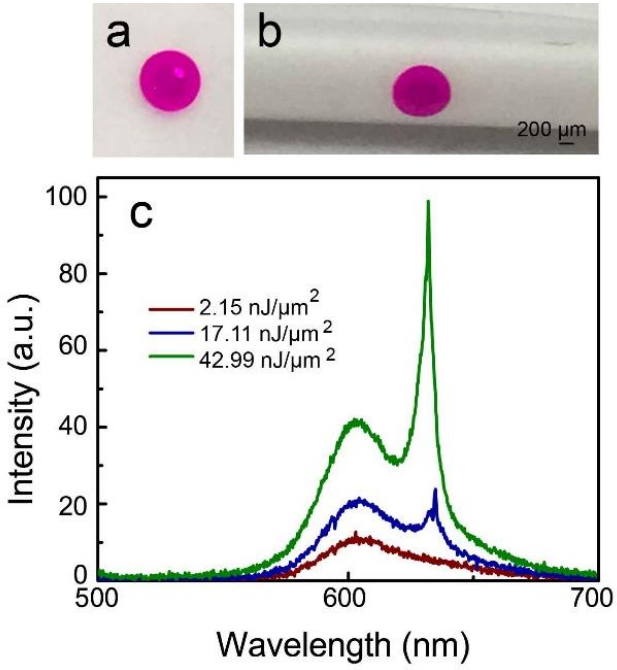

Figure 4.18 (a) RhB–PVP disk structure on a flat and **(b)** rolled tape (MAS® Invisible). **(c)** The emission spectrum of a rolled RhB–PVP disk at different pump intensities.

Chapter 5

SELF-ASSEMBLED SPATIALLY LOCALIZED FEEDBACK LASERS

In this chapter, we fabricated self-assembled films with cracks and utilized them as SLF based RLs. In the first section, self-assembled microstructural cracks that are spontaneously formed upon radial strain-release of colloidal nanoparticles from wet to dry phase. In the second section, we fabricated uniform films using self-assembly and applied mechanical stress by bending the film to obtain nanocracks. In both sections, the cracks are utilized as diffuse reflectors, and between two consecutive cracks, a microcavity is formed that supports SLF based RLs.

5.1 Spatially Localized Feedback Lasers using Self-assembled Cracks

In this section, we demonstrated SLF based RLs using cracks oriented in a radial direction. We made RLs from a wide variety of nano and biomaterials including silica nanoparticles, fluorescent proteins, and biopolymers. These microlasers are created by strain release that spontaneously induces cracks with rough sidewalls. Normally undesired crack sidewalls work well as diffusive reflectors; and output coupling occurs at the crack sidewall-air interface. Diffuse reflection from these sidewalls results in light oscillation in the pumped gain medium and lasing directionality that is quasi-orthogonal to the unparalleled crack boundaries.

5.1.1 Self-assembly of Cracks

The self-assembled cracks are fabricated via room-temperature drying of droplets that consist of Rhodamine B (RhB) as the gain medium, 13-nm silica nanoparticles as the crack-forming dielectric medium, and methyl ethyl ketone (MEK) and acetonitrile as the solvent.

After the droplet is cast on a glass, the perimeter of the droplet pins to the glass surface. Although the solvent evaporates from the droplet surface, evaporation is faster at the perimeter[4] where the droplet is thinnest. During the evaporation, the particles are carried to the edges by the outward radial flow of the solvent (Figure 5.1). The faster solvent evaporation near the pinned contact line concentrates the particles close to the droplet edge. Micron-sized particles tend to form a few lines of stacked particles at the perimeter, resulting in a well-known 'coffee-ring' pattern [4]. Nanoparticles, on the other hand, can form multilayered close-packed arrays [44]. In the late stages of the drying process, the receding contact line induces tensile stress on the nanoparticle film, which eventually cracks to release the internal stress [45]. While the final crack pattern depends highly on the size and softness (shear modulus) of nanoparticles [46], film thickness, and particle packing ratio, highly periodic and radially oriented cracks are often observed for rigid spherical nanoparticles [47, 48].

Figure 5.1 Transformation of silica nanoparticle solution into a cracked pattern.

The drying induced cracks of nanoparticles are often considered as undesirable defects [49], here we use them as diffusive reflection sides (Figure 5.2 and b), which function as resonator cavities that support SLF based RLs (Figure 5.3).

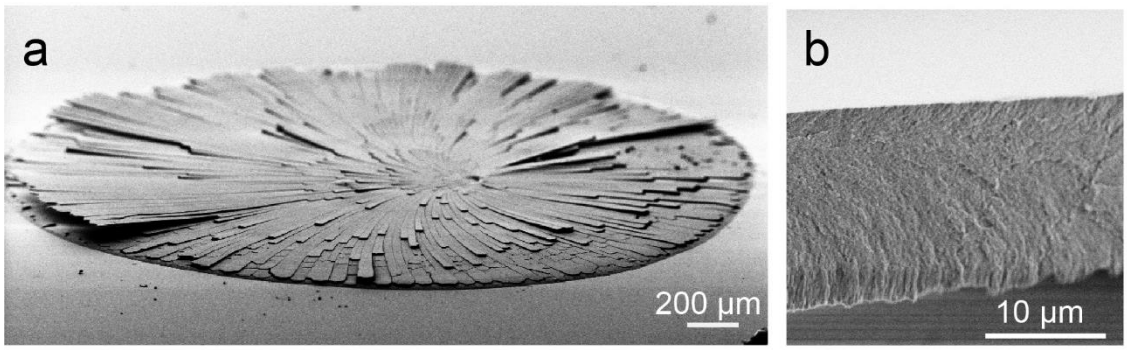

Figure 5.2 SEM image of **(a)** crack patterns and **(b)** their rough sidewalls.

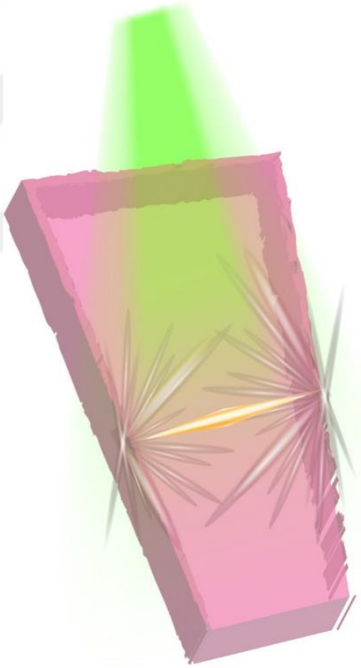

Figure 5.3 Schematic illustration of cracks supporting SLF based RL modes.

5.1.2 Laser Light Generation by Cracks

To investigate the emission characteristics of self-assembled structures, the selected area of the microstructure (Figure 5.4-a) was pumped with pulses generated by an optical parametric

oscillator (10 Hz, 5 ns) (Figure 5.4-b). The pump wavelength was set to 535 nm within the absorption band of RhB for population inversion (Figure 5.4-c). Spectral emission patterns of the cracks below and above threshold were investigated corresponding to pump energy densities of ~40.6 and 253.8 μJ/mm^2, respectively (Figure 5.4-d and e). While the subthreshold emission pattern exhibits spectral uniformity and weak intensity, at pump power above the lasing threshold, narrower spectral lines emerge with much higher intensities. The emission spectrum of a cracked sample is illustrated at different pump energy densities (Figure 5.4-f). The Q-factor (*Q)* is calculated from the ratio of the peak emission wavelength

$$Q = \lambda_{Peak} / \Delta\lambda \tag{5.1}$$

where λ_{Peak}=587 nm and the emission linewidth $\Delta\lambda$=39 pm, and is equal to 15,051. Moreover, the integrated emission intensity also shows a threshold behavior and increases significantly faster at pump powers above ~88 μJ/mm^2 (Fig 5.4-g). These observations support laser emission characteristics. We investigated the side facets of the cracks and since the cracks are established by the stress relief, the side-facets are rough and scatter the light. Each microstructure creates a local optical path between the boundaries of the cracks, which is surrounded by air. In addition to their roughness, the consecutive side facets are also not parallel to each other. Therefore, these rough and non-parallel facets cannot support Fabry–Pérot resonances based on specular reflection. Yet, these boundaries can form SLF for the gain medium. Hence, the boundary can simultaneously lead to diffuse reflection from the scattering crack boundaries, as well as out-coupling the generated laser light.

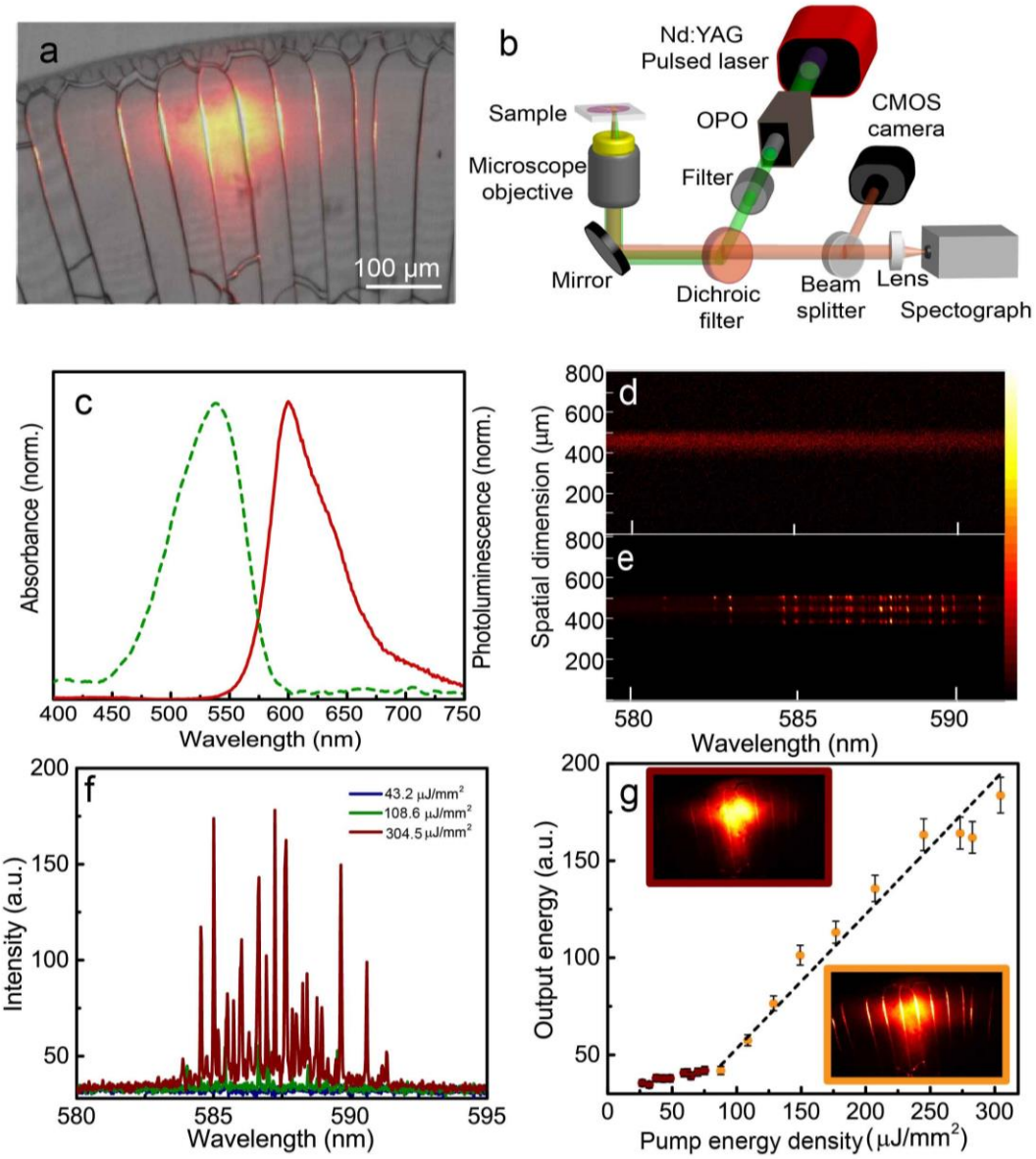

Figure 5.4 (a) Optical microscopy image with overlayed emission intensity of silica deposited microparticle crack pattern, with pump beam illuminating the region where lasing appears above threshold. Laser emission is detected from bright diffuse cracks. **(b)** Optical set-up used in RL experiments. **(c)** The absorption and emission spectrum of RhB doped silica film. Emission of cracks in the spatial pattern **(d)** below and **(e)** above threshold. **(f)** Emission spectrum of the cracks at different pump energy densities and **(g)** corresponding output energy of emission in terms of pump energy density. Inset: Optical image of the pumped area below and above threshold energy respectively.

5.1.3 Mode Analysis and Numerical Simulations

To explore the effect of the crack structures on the laser emission spectrum, we pumped cracked microstructures of different inter-crack distances and compared their emission profile with the calculated mode wavelengths using

$$\lambda = 2n_{silica}L/m \tag{5.2}$$

formula, where λ is the wavelength, n_{silica} = 1.46 is the refractive index of our host medium [50], L is the distance between two cracks and m is the mode number. First, two microstructures are simultaneously pumped (Figure 5.5-a) and dominant modes appear at 580.45, 581.81, 582.40, 583.8, 583.97 and 584.67 nm (Figure 5.5-b) while theoretical calculations are shown in Figure 5.5-c from 580 nm to 585 nm. Theoretically, 60.4 μm crack zone supports the wavelengths at 580.29, 582.20 and 584.12 nm with a free spectral range (FSR) of 1.6 nm. On the other hand, in experimental results, the FSRs are 1.95 nm and 1.57 nm. Likewise, 73.0 μm zone calculations result in the wavelengths at 580.21, 581.80, 583.40 and 584.99 nm with 1.9 nm FSR. However, when we compare the experimental results and the calculated wavelengths, we observe that the results are not in agreement as the FSRs vary and the modes do not agree with the Fabry–Pérot equation. Accordingly, we observe that the cracks support SLF based RLs.

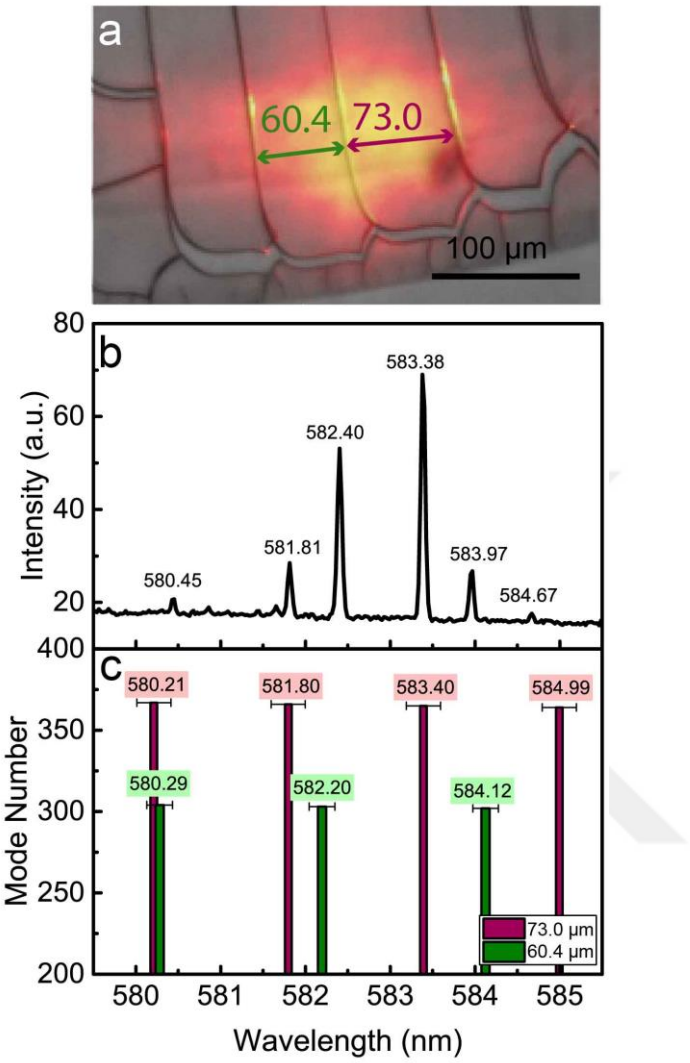

Figure 5.5 (a) Optical microscopy image with an overlayed emission intensity of RhB doped silica crack patterns when two microstructures are pumped. The pumped regions are marked with two-sided arrows. **(b)** Emission spectrum of microcavities. **(c)** Theoretical mode analysis of green and red-colored arrows.

To sustain the phenomena that non-parallel crack side-facets constitute an RL, we examined the emission properties of RhB doped colloidal silica droplet until it transforms into a cracked pattern. There is a time slot between solvent evaporation and crack formation. In this time interval, lasing was not observed until crack formation (Figure 5.6).

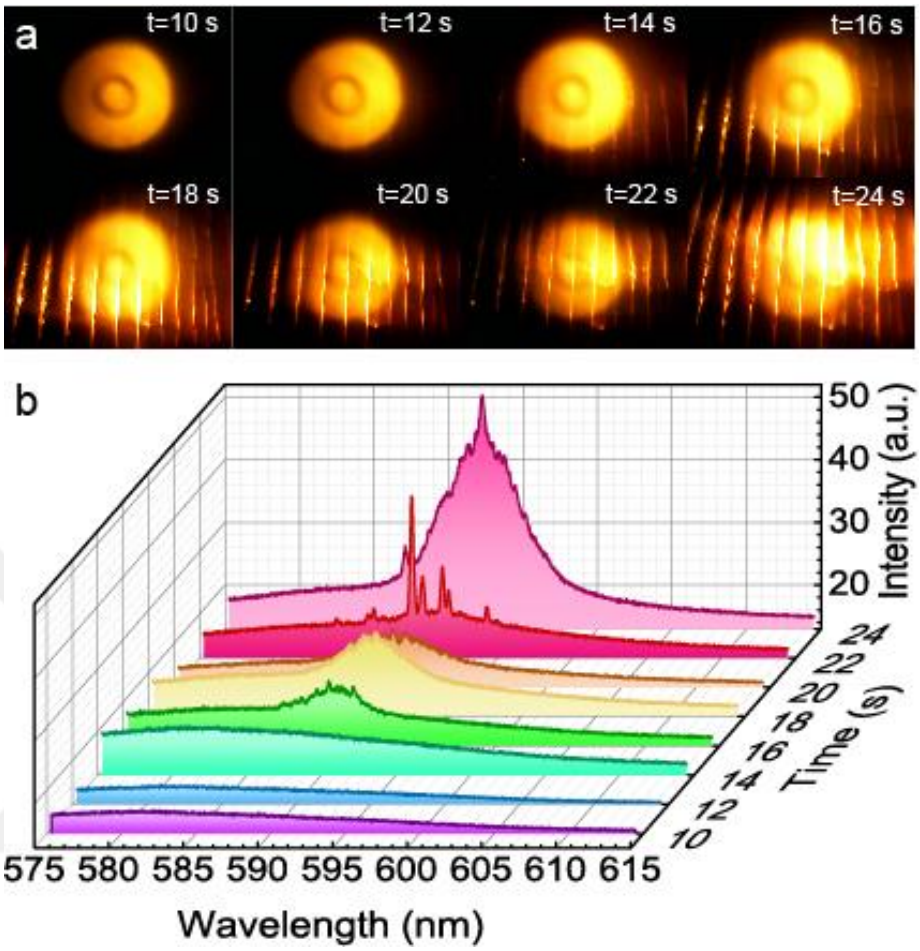

Figure 5.6 (a) Transformation of SiO_2 solution to SiO_2 cracked patterns with respect to time under pump laser and **(b)** their emission spectrum at equal time intervals.

5.1.4 Directional Random Lasing

The silica crack patterns have high periodicity in a radial direction. Each zone between two consecutive cracks performs as a single microcavity since cracks are lined up next to each other with an air gap in between them (Figure 5.7-a). We pumped the radially oriented cracks using a deltoid beam with vertical symmetry to prevent the effect of the pump beam shape. The narrow peaks arose in the emission graph indicating the SLF based random lasing (Figure 5.7-b). The in-plane emission directionality was estimated by the far-field pattern of light intensity (Figure 5.7-c). During laser action, emission that is orthogonal to the crack sidewalls was observed with an angle of divergence of 24º (Figure 5.7-d). Moreover, the

emission is also partially coupled to the microcavities, which behave as optical waveguides as well.

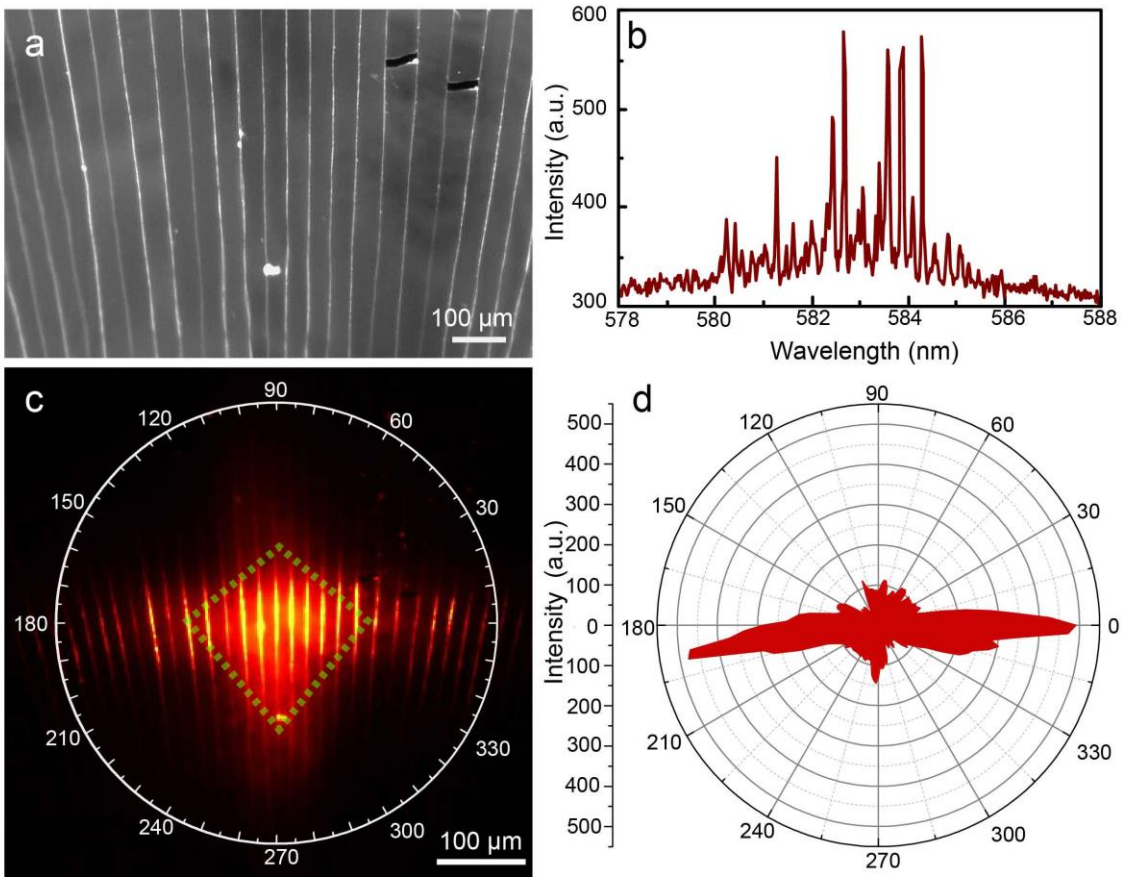

Figure 5.7 (a) Fluorescence image of RhB doped silica cracks and **(b)** their laser emission spectrum. **(c)** The optical microscopy image of cracks while lasing. The dashed green lines show the pumped area. Angle marks are included. **(d)** The intensity of the emission profile as a function of the angle.

Previously, in SDF based RLs consisting of distributed scattering points, the shift in output spectrum was studied by adding more scattering particles to the system [51]. In the coffee stain effect, the residue formation depends on both the particle size [41] and shape [52]. In our structure, given that the structure is formed by the coffee stain effect, the gain and thickness change with the position. To map the emission features of cracks (Figure 5.8) in

terms of the position, we utilized an automated system to shift the sample in one direction periodically and measured the photoluminescence of cracks at each position.

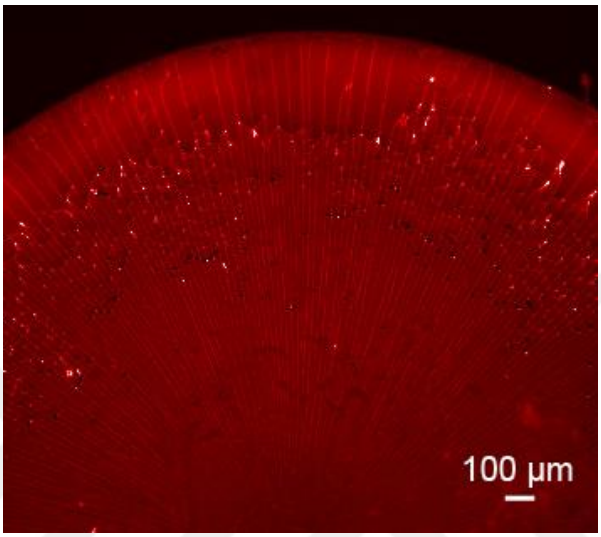

Figure 5.8 Fluorescent image of RhB doped silica cracked pattern.

The optical microscopy image of the cracked pattern is shown in Figure 5.9-a where the dashed green arrow shows the direction of the pump laser scan. The spectra images were taken along ~160 µm line in steps of ~4 µm. We illustrate the emission spectrum under the threshold pump power to check the gain medium distribution according to the position (Figure 5.9-b). The emission spectrum blue shifts from 574.5 nm to 571.7 nm at 120 µm distance and red shifts to 572.1 nm at 140 µm. Next, we increased the pump power density above the threshold and the position-dependent output spectrum is measured along 160 µm (Figure 5.9-c). High-intensity points with non-uniform distribution represent the random lasing based on domains between cracks. We plot the output spectra at each 20 µm in terms of wavelength extracted from Figure 5.8-c while the inset images illustrate the pumped area of the cracks while the insets show the optical image of cracks under pump light (Figure 5.9-d). When we compare the gain emission spectrum with RL modes, we observe that the shift behavior is in agreement (~4 nm).

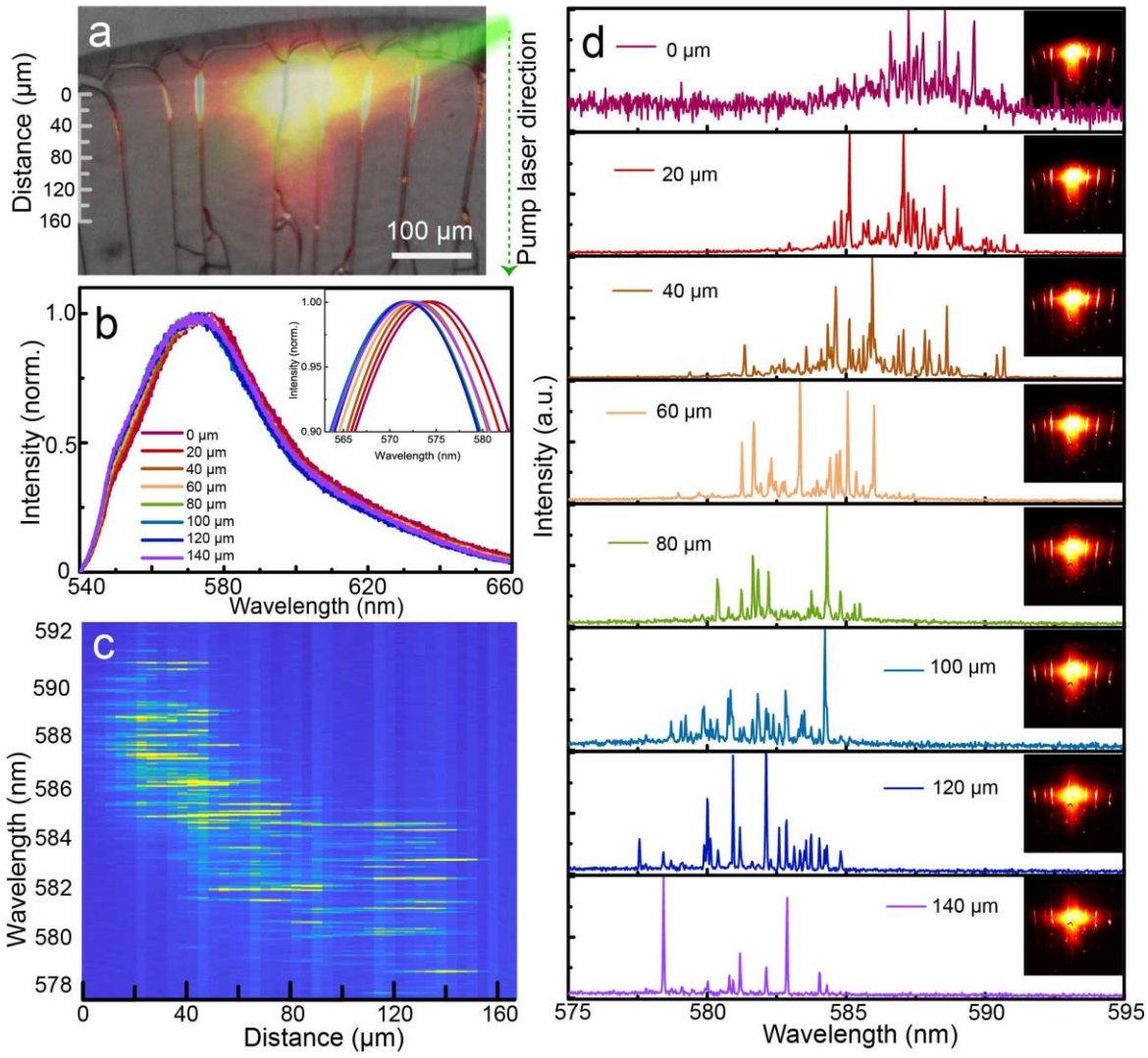

Figure 5.9 (a) The optical microscopy image with an overlayed emission intensity of RhB doped silica cracks with marked laser scan direction to investigate laser wavelength emission dependence with the structure width **(b)** Emission spectrum of shifted points below the threshold. Inset shows the zoomed view of the fitted peaks. **(c)** Emission spectra along the scanned line of a single microstructure that becomes narrower at greater distances. **(d)** Emission spectrum of shifted points shown at each 20 μm measured above the threshold. The inset shows the camera image while the cracks lase random.

5.1.5 Laser Light Generation by Biomaterial Cracks

GFP has been widely used in biology and medicine for imaging and studying processes in cells and whole organisms. Since fluorophores of GFP are surrounded by β-barrels, (Figure 5.10), their luminescence is more stable than other fluorescent dyes. With these protective shields, bioluminescent proteins are quite suitable optical gain material for lasers. To date, GFP expressing cells [53], solid-state GFP films [8], or rod-shaped GFP crystals [54] were inserted in between mirrors, and their lasing properties were investigated [8, 53, 54]. Furthermore, GFP is doped in SF protein and whispering gallery mode lasers [31] and distributed feedback lasers [26] were built. Here in this study, we made a GFP RL utilizing similar cracks as above. Since GFP is a bioluminescent protein, we can simultaneously use GFPs as the gain and cavity material without adding it into a host material.

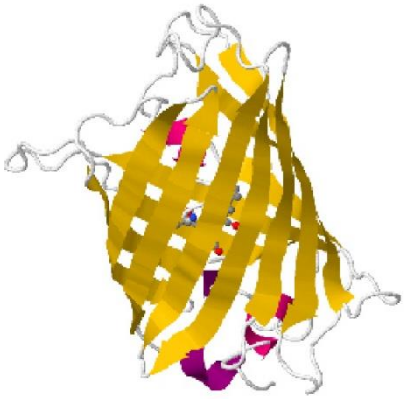

Figure 5.10 Schematic GFP structure [55].

To create GFP crack-based microstructures, we used aqueous GFP solution. 7 wt% 5 µl GFP solution was dripped on a glass slide and heated inside a 50ºC oven to evaporate water and we obtained cracked GFP stain. The GFP crack formation is illustrated in Figure 5.11.

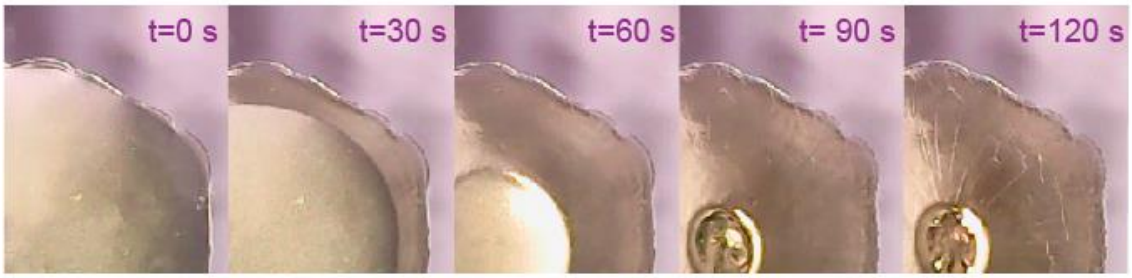

Figure 5.11 Transformation of aqueous GFP solution to the cracked pattern at 50ºC.

The absorption and emission spectra of the solidified and cracked GFP film (Figure 5.12-a) is illustrated in Figure 5.12-b.

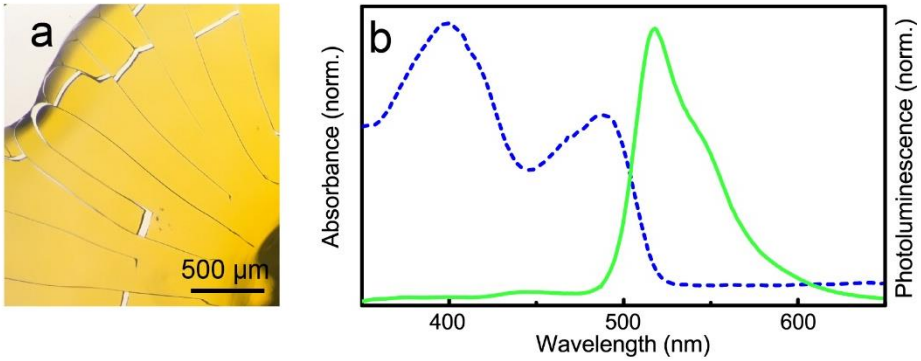

Figure 5.12 (a) Optical microscopy image of GFP crack patterns. **(b)** Absorbance and photoluminescence spectrum of GFP cracked film.

The measurement area for RL experiments is marked with a red, dashed circle in white light interferometry (WLI) image of the cracked GFP layer (Figure 5.13-a). To excite the GFP crack interfaces, we used a 521 nm pump laser wavelength and a 500 nm long-pass filter. We pumped this area with different pump energy densities and observed narrow spectral peaks above ~68 µJ/mm^2 pump power (Figure 5.13-b and c). Then, we separated GFP from the crack boundaries to obtain individual GFP pieces and studied their emission properties

(Figure 5.13-d). With this separation, we obtained the SLF based random lasing where the light emission is confined within the cracked sidewalls (Figure 5.13-e). To further investigate the GFP based RLs, we examined the time-dependent intensity of the GFP crack pattern. To measure this, an ordered GFP crack zone was pumped for 40 minutes with a 10 Hz pulsed laser at 136.5 μJ/mm^2 pump energy density (Figure 5.13-f). Since the β-barrels in the GFP (Figure 5i inset (left)) prevent photobleaching when the GFP is in the form of a solid film[54], the integrated emission field remained almost constant and the emission intensity was maintained for 40 minutes under 10 Hz excitation with a mean decrease less than 15%.

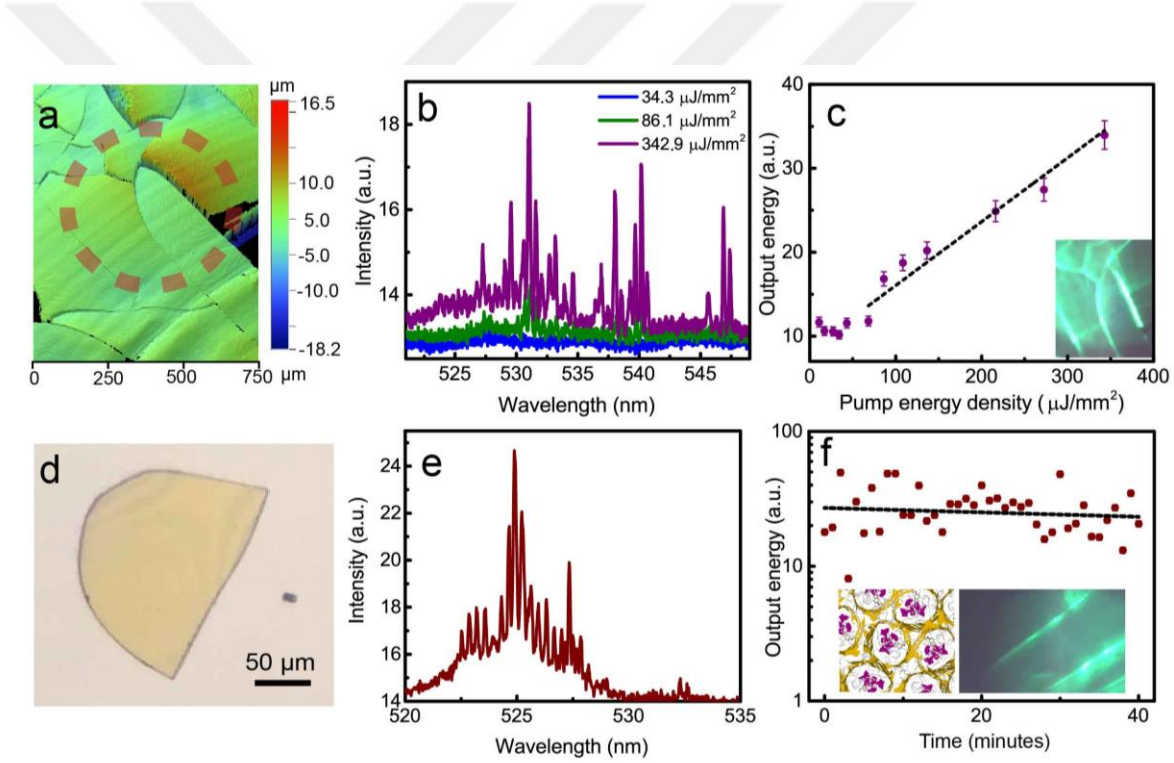

5.13 (a) Image of GFP film thickness using WLI. Dashed circle marks the probed area for laser emission. **(b)** Emission spectrum of the marked area at different pump energy densities. **(c)** Output power of cracked GFP as a function of pump energy density. Optical image of GFP sample when it is pumped by 483 nm laser above threshold. **(d)** Optical microscopy image of an eGFP crack and **(e)** its emission spectrum. **(f)** Integrated emission intensity of GFP cracks with respect to time when it is pumped at 136.5 μJ/mm^2. Inset shows the simplified sketch of packed GFP and optical image of the pumped area during emission, respectively.

To motivate our method and its potential to utilize a different kind of materials, we repeated the experiments with another biopolymer. We prepared Rhodamine 6G (R6G) doped PVP cracks patterns. PVP is a biocompatible and biodegradable polymer commonly used in medicines. To obtain a crack pattern from PVP, the aqueous PVP solution was doped with R6G and 100 µl of the solution was drop cast on a glass slide. The deposit, which was kept in the 200°C oven for 5 minutes, had a very smooth surface when removed from the furnace. The cracking starts after the deposit moved out from the furnace (Figure 5.14).

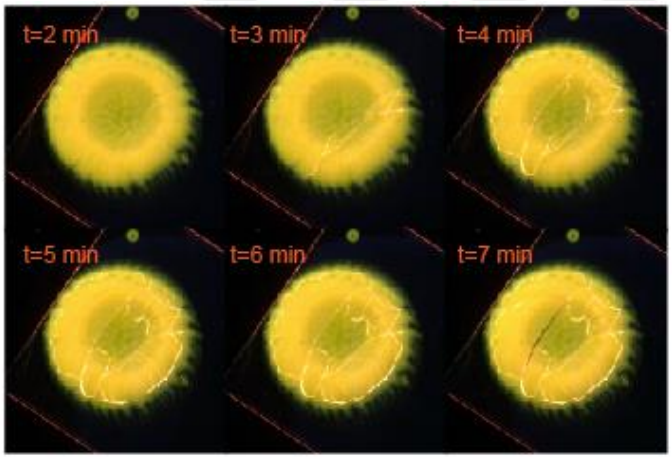

Figure 5.14 Crack formation by stress relief from R6G doped PVP.

We showed that these cracks can also successfully generate SLF based random lasing. The PVP cracks (Figure 5.15-a) absorption and emission spectrum are shown in Figure 5.15-b. Figure 5.15-c shows the WLI image of the sample that we measured lasing where the dashed circle shows the pumped area. We observed lasing after ~38 µJ/mm^2 (Figure 5.15-d and e).

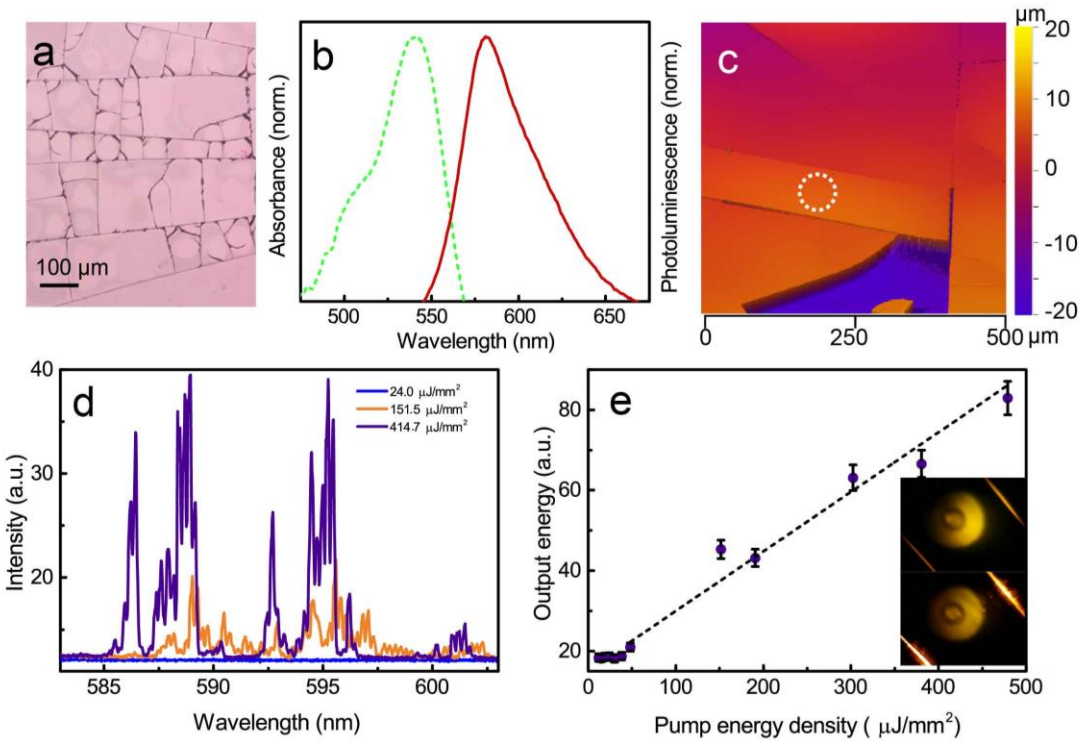

Figure 5.15 (a) Optical microscopy image of R6G doped and cracked PVP film. **(b)** The absorption and emission spectrum of R6G doped PVP film. **(c)** WLI image of the PVP crack pattern. **(d)** Emission spectrum of PVP cracks and **(e)** integrated output energy of these cracks with respect to pump energy density. Inset shows the images of the cracks below and above threshold pump power densities respectively.

5.2 Spatially Localized Feedback Random Lasers Using Cracks Formed on Self-Assembled Biopolymer Films

This section explains the lasing properties of self-assembled SF films applied to stress-induced cracking. Nanocracks are oriented in parallel and the structure resembles the gratings with rough sidewalls. A microcavity is formed between two cracks and the periodicity of the structure result in directional emission.

5.2.1 Silk Fibroin Nanocrack Formation

Aqueous SF solution is doped by the optical gain material of Rhodamine B (RhB) and the biopolymer-dye solution is poured on a petri dish substrate and treated with heat at 60° C in the oven. The dried free-standing SF film (~11 µm-thick) is cut in a rectangle shape (1 cm x 4 cm) (Figure 5.16-a), folded (Figure 5.16-b) and twisted for nanocrack formation by 2 mm radius of curvature (Figure 5.16-c and d). Bending and rolling were used for applying uniform bending stress to generate nanocrack on a relatively large area sample. As a result, parallel nanocracks extending uniformly along the twisted zone are produced (Figure 5.16-e and f). The size distribution of microcavities corresponds to an average length of 6±1.7 µm (Figure 5.16-g) and the sidewalls between the cracks are around 182 nm (Figure 5.16-h).

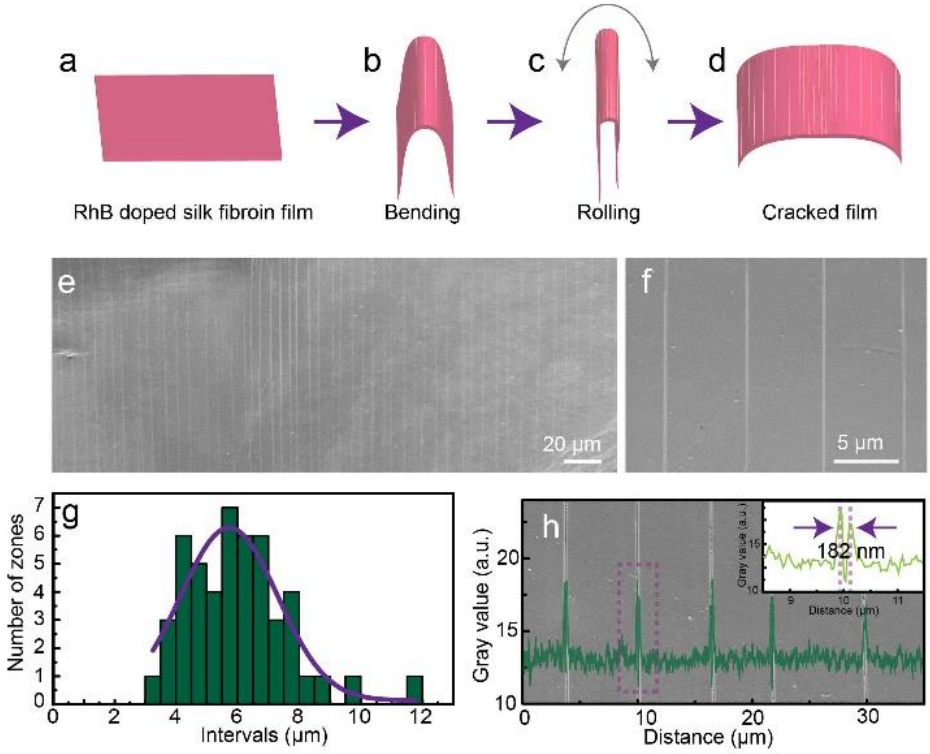

Figure 5.16 (a-d) Schematic process flow for SF nanocrack formation. **(e-f)** SEM images of SF nanocrack films. **(g)** Length distribution of microcavities. A total of 49 microcavities was counted. **(h)** Image analysis of nanocrack width. Inset: Zoomed version of an exemplary nanocrack interval.

5.2.2 Random Lasing of Nanocracks

To determine suitable pump wavelengths, we measured the absorption and emission spectrum of our gain medium (Figure 5.17-a). We used a 10 Hz and 5-8 ns pulsed Nd: YAG laser that was set the pump wavelength to 520 nm to pump the microcavities (Figure 5.17-b). To understand the role of the nanocracks in RL emission, we prepared SF films with and without nanocracks. We excited these free-standing SF films at different pump powers from ~1.8 to 141.4 μJ (Figure 5.17-c and d). While the crack-free film emits a broad spectral range emission, narrow spectral peaks started to be observed by the cracked film after a definite pump power of ~23 μJ. Furthermore, the integrated emission intensity increases linearly in the crack-free SF film, whereas nanocrack originated microcavities show a threshold behavior (Figure 5.17-e). The optical microscopy image of free-standing films without and with cracks are shown in the inset of Figure 2e, at pump energies of below and above threshold energy of nanocrack lasing, respectively, and the change of the laser emission directionality above the threshold is also clearly visible. Here, RL light is formed by spatially localized feedback (SLF), which uses scattering zones on the edges of the gain medium[18, 56]. In our structure, two sequential crack forms a single SLF based RL microcavity and the scattered light oscillates between the nanocracks for laser light generation (Figure 5.17-f).

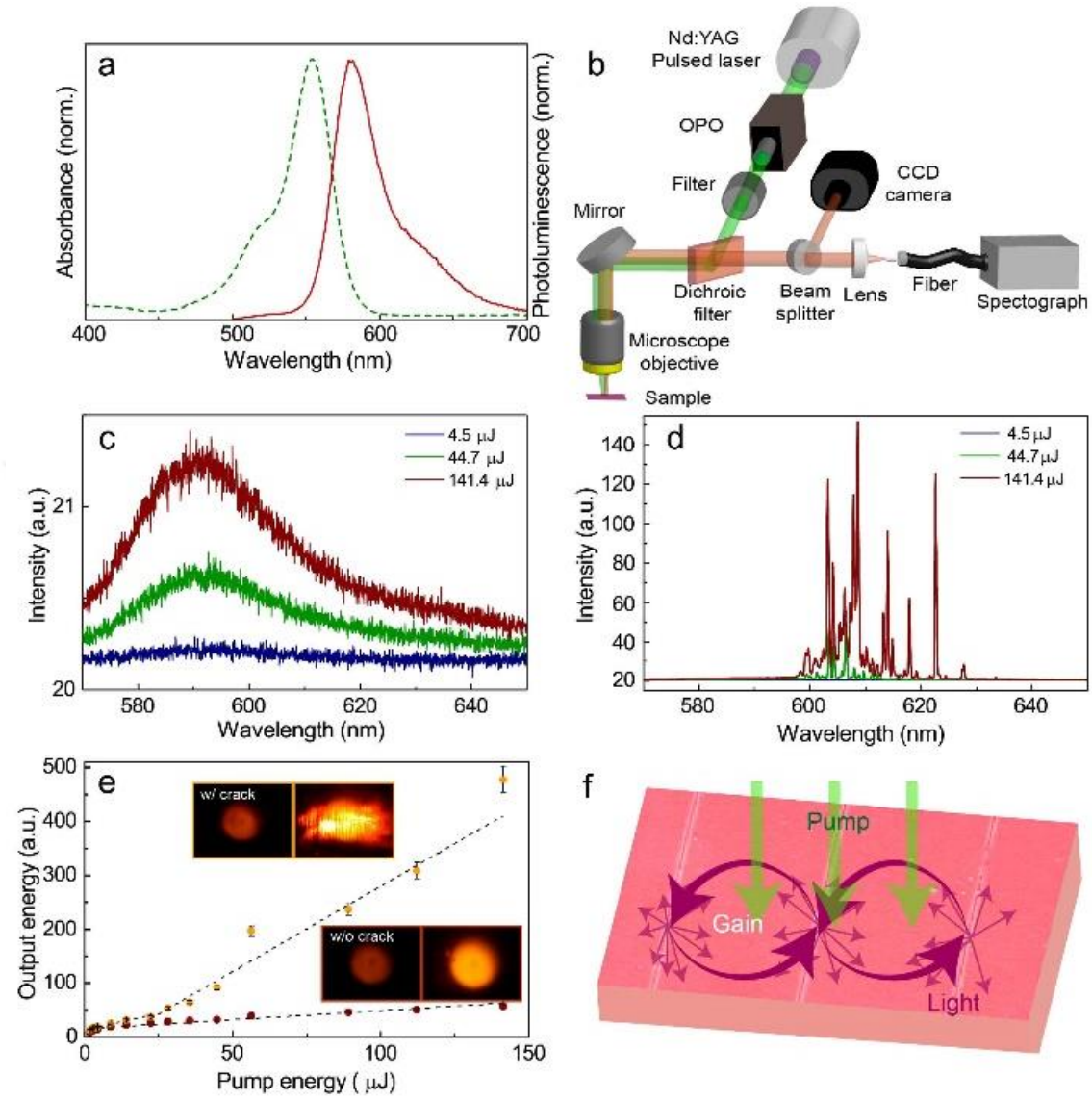

Figure 5.17 (a) The absorption and emission spectrum of RhB inside water. (b) Schematic of the optical set-up used in RL experiments. Emission spectrum of SF film (c) without and (d) with nanocracks at different pump energy densities, (e) their corresponding output energy of emission in terms of pump energy, respectively. Insets: Optical images of the pumped area below (left) and above (right) threshold energy, respectively. (f) Schematic diagram of SLF based nanocrack RL (not drawn in-scale).

5.2.3 Directionality of laser emission

We performed 2D numerical simulations using a finite-difference time-domain (FDTD) method in *Lumerical* to check the possibility of directional laser emission via nanocracks. In our model, the nanocracks having an interval of 180 nm are introduced to the SF (n_{silk}=1.54) with an interval of 6 μm (Figure 5.18-a). The rough surfaces were predefined using 500 nm correlation length both in x and y-directions and 50 nm root mean square (RMS) amplitude and the simulation is characterized using bidirectional scattering distribution function (BSDF) [57]. Gaussian beams injected into the system with a 2 μm beam radius and perfect matching layers applied as boundary conditions to analyze the non-specular scattering. Rough surfaces enhance diffuse reflection and the introduction of diffuse reflectors transfer the generated laser light with high directionality (Figure 5.18-b). Moreover, the laser modes by the nanocracks were also visible (Figure 5.18-c).

We investigated the directionality of the SF RL. For that, we pumped an array of microcavities (Figure 5.18-c) and generated laser emission (Figure 5.18-d). We observed in-plane directionality with a narrow divergence angle of 17° (Figure 5.18-e). So far, silk RLs have omnidirectional output in spatially distributed feedback (SDF) systems that have random scatter inside the gain medium [58-61]. Differently, in this study, the rough parallel side walls are the scatterers, which simultaneously bounces back the light to the pumped gain medium and out-couple from the microcavity to the air facets. In this way, laser light can propagate with high directionality.

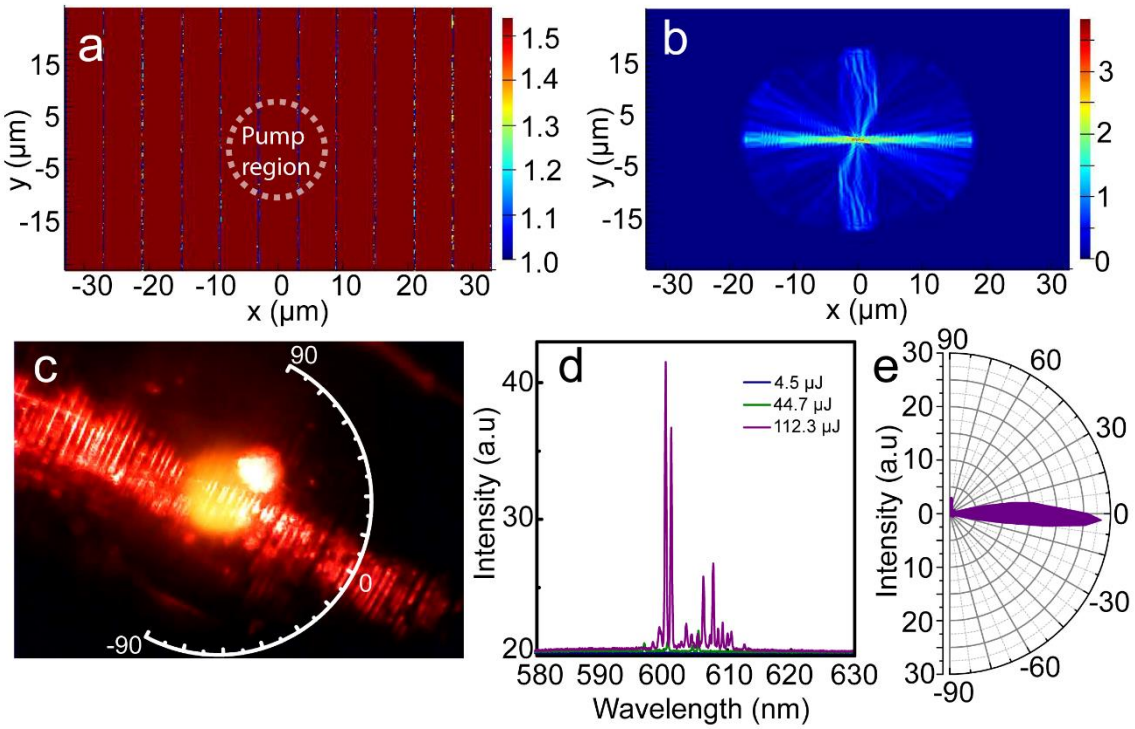

Figure 5.18 Simulation results of **(a)** effective refractive index of microcavities and **(b)** their electric field profile. **(c)** Optical image of nanocracked SF film under pump beam and **(d)** its emission profile at the pump energy of ~64 μJ. (**e)** The angular emission profile.

Chapter 6

SINGLE TRANSVERSE MODE AND ALL PROTEIN DISTRIBUTED FEEDBACK LASER

Reproduced (adapted) from I. B. Dogru et al., "Single transverse mode protein laser," Applied Physics Letters, vol. 111, no. 23, p. 231103, 2017. *with permission of AIP Publishing.*

Here we report a single transverse mode DFB biolaser. The gain medium that is composed of eGFP in an SF yields a waveguiding gain layer on a DFB resonator. The thin titanium dioxide (TiO_2) layer on the quartz grating improves optical feedback due to the increased effective refractive index [26].

6.1 Grating Fabrication

For the fabrication of the quartz grating, the template was fabricated on square-shaped quartz samples of 1×1 cm^2. First, a 50 nm thick Cr layer was deposited on the cleaned quartz sample using an e-beam evaporator (ZZS550-2/D, Maestech). A negative photoresist (AZ nLOF 2070, Microchemicals) was then spin-coated on the Cr surface with a thickness of 250 nm by controlling spin-coating speed to 4000 rpm, followed by post-baking at 95 °C for 1 min. Further, the sample was subjected to laser beam interference to generate a 1D diffraction grating pattern by the laser holography lithography (LHL) method (Figure 6.1-a). The LHL system mainly consists of a 266 nm diode-pumped solid-state source laser (FQCW266-50, CryLas), a spatial filter, and a Lloyd's mirror stage. The desired duty cycle and grating period were controlled by the exposure time and incident beam angle. The exposed sample was baked at 100 °C for 1 min and then the exposed resist was developed. The resist pattern was transferred to the underlying Cr-deposited quartz substrate using reactive-ion etching (RIE) equipment (RIE 80 plus, Oxford Instrument). The quartz grating was obtained by the conventional Cl_2, CF_4-based RIE process, and the residual Cr layer was removed by wet-

etching. Figure 6.1-c shows the AFM image of the DFB grating with a grating period of 330 nm.

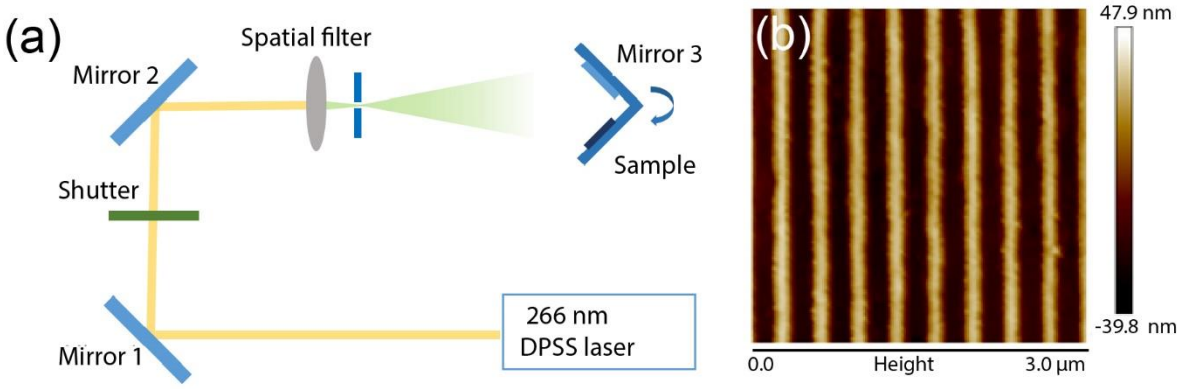

Figure 6.1 (a) Schematic of LHL setup. The LHL setup mainly consists of 266 nm diode-pumped solid-state source laser, a spatial filter, and a rotational stage. **(b)** AFM image of DFB quartz grating with 330 nm pitch size.

6.2 Numerical Analysis of Distributed Feedback Laser

Numerical simulations were performed by FDTD solution, Lumerical. Two-dimensional FDTD simulations were performed with the Bloch boundary condition (k_x =0) in the *x*-direction, while the perfect matching layers were applied along the top and bottom in the *y*-direction. The TiO_2 periodic surface was excited by setting multiple random poles to excite the periodic unit cell structure. RIs of 1.54 (SF), 1.50 (quartz), and 2.45 (TiO_2) were used in the modeling. We obtained spectral and spatial data of the magnitude of the electric field by setting time conditions of 3,000 fs.

A second-order grating was employed in the fabricated DFB laser structure. The grating pitch size (Λ) of 330 nm was chosen to induce a second-order Bragg resonance wavelength ($\lambda_{Bragg} = \Lambda n_{eff}$, with n_{eff} being the effective refractive index of the waveguide mode) within the photoluminescence (PL) emission spectrum of the eGFP. Figure 6.2-a and b show the simulated spectra and field profiles for the DFB structure made on a quartz substrate

according to the designed parameters for the second order DFB laser with the pitch size of (Λ) of 330 nm, the grating depth of 65 nm with 60 % duty cycle and the 200-nm thick gain layer. However, in this structure the electric field is leaky to the quartz substrate due to the small index contrast between the quartz and the gain medium.

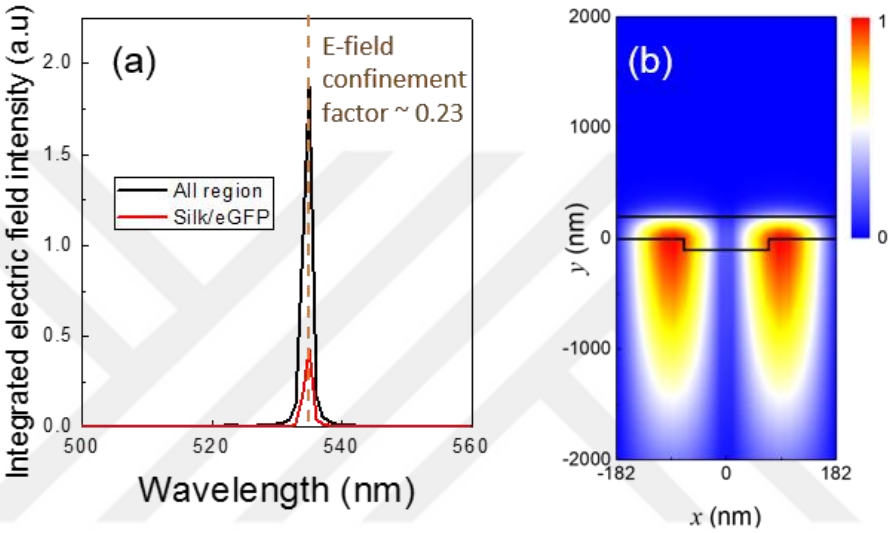

Figure 6.2 (a) Spatially integrated electric field intensity in all the simulated region (black solid line) and in the optically active silk/eGFP film (red solid line) of the DFB structure. (b) The electric field profiles of resonance TE modes (l ~ 534 nm).

To achieve lasing, it is important to have sufficient optical gain in comparison with the optical losses. Therefore, it is critical to obtain strong optical feedback by an optical resonator. In order to enhance field localization in the gain medium, a thin TiO_2 layer with a higher refractive index was deposited on the surface of the quartz grating. Applying a very thin TiO_2 layer to the silk/quartz interface induces a narrower field profile of the waveguide mode around the interface and therefore optical feedback and confinement are increased. The confinement factor of the electric field in the silk gain layer, defined in Equation 6.1 [62] was almost doubled when the TiO_2 layer was applied, due to the increased n_{eff} (Figure 6.3-a). Therefore, it is important to use a TiO_2 layer on quartz grating.

$$\text{Electric field confinement factor} = \frac{\int_{silk/eGFP}|E|^2 dA}{\int_{all\ region}|E|^2 dA} \quad (6.1)$$

The main peak at 534.2 nm, shown in Figure 6.3-b, corresponds to TE polarization (with the magnetic field vertical, normal to the grating surface, and with the electric field parallel with the grating lines), and illustrates that the perturbation produced by the TiO_2 layer influences the coherent feedback provided by the grating structure. The TM resonance mode was investigated corresponding to satellite peak at 500.2 nm in Figure 6.3-c. The blue-shifted resonance of the TM mode is due to a lower n_{eff} of the grating for the TM mode than for the TE mode, which is induced by different border conditions for TE and TM modes at the grating interfaces.

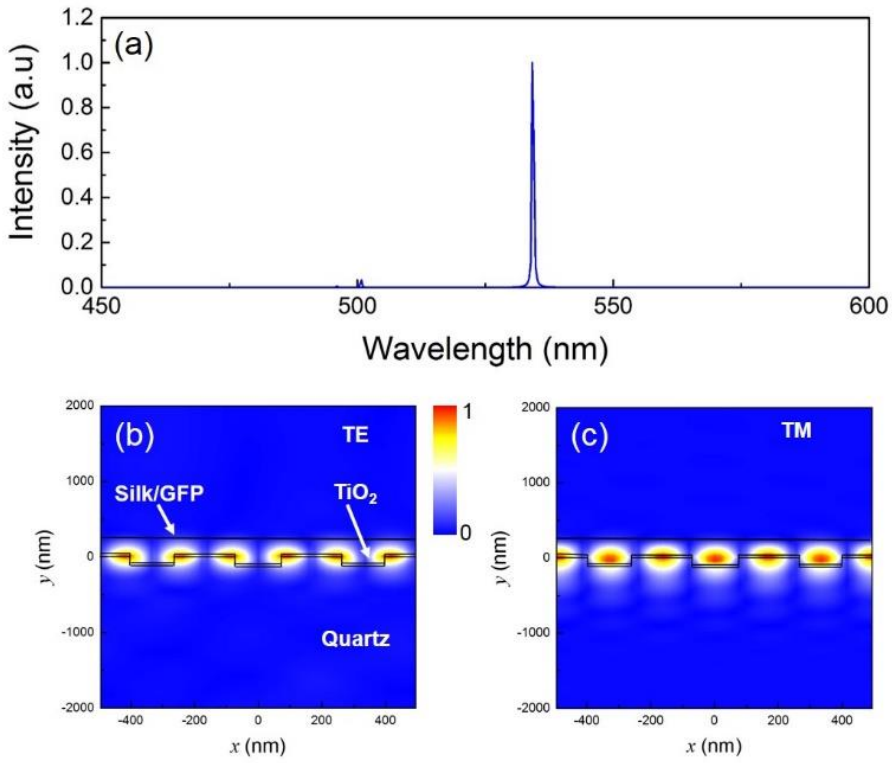

Figure 6.3 (a) Simulation results for 200 nm thick eGFP/SF gain layer with TiO_2 in the DFB structures. Simulated spectrum results showing the resonance peaks. The normalized electric field profiles corresponding to the resonance mode at **(b)** 534.2 nm and **(c)** 500.8 nm, respectively

6.3 Experimental Analysis of Distributed Feedback Lasers

eGFP shows a quasi-four level laser system as shown in Figure 6.4-a, where the ground (S_0) and excitation state (S_1) include sub-energy levels [53]. In this laser system, the optical pump excites the molecule at S_0 to the S_1 that populates the molecule in the excited state [63]. Afterward, the molecule relaxes quickly to the lowest energy level in S_1, which is a long-lived state with a lifetime of about 1.7 ns (MicroTime 100, Picoquant) (Figure 6.4-b). Thus, at sufficiently-high pumping levels the transition between S_0 and S_1 levels result in population inversion and stimulated emission.

For population inversion, Quanta-Ray INDI pulsed Nd: YAG laser is used with a typical pulse width of 7 ns and a repetition rate of 10 Hz. The excitation wavelength is adjusted as 483 nm by OPO (Basiscan, SpectraPhysics) due to the strong absorption of eGFP at this wavelength (Figure 6.4-c). The pump that is generated by the OPO passes through optical density filter for laser transmission adjustment (Figure 6.4-d). After the pump signal arrives at a 500 nm long pass dichroic filter, the dichroic filter reflects the pump laser and it passes through a cylindrical lens to have a line-shaped laser beam on the sample. Since the emitted light from the sample has a longer wavelength than 500 nm, it passes through the dichroic filter and reaches to the spectrometer (Torus Concave Grating Spectrometer).

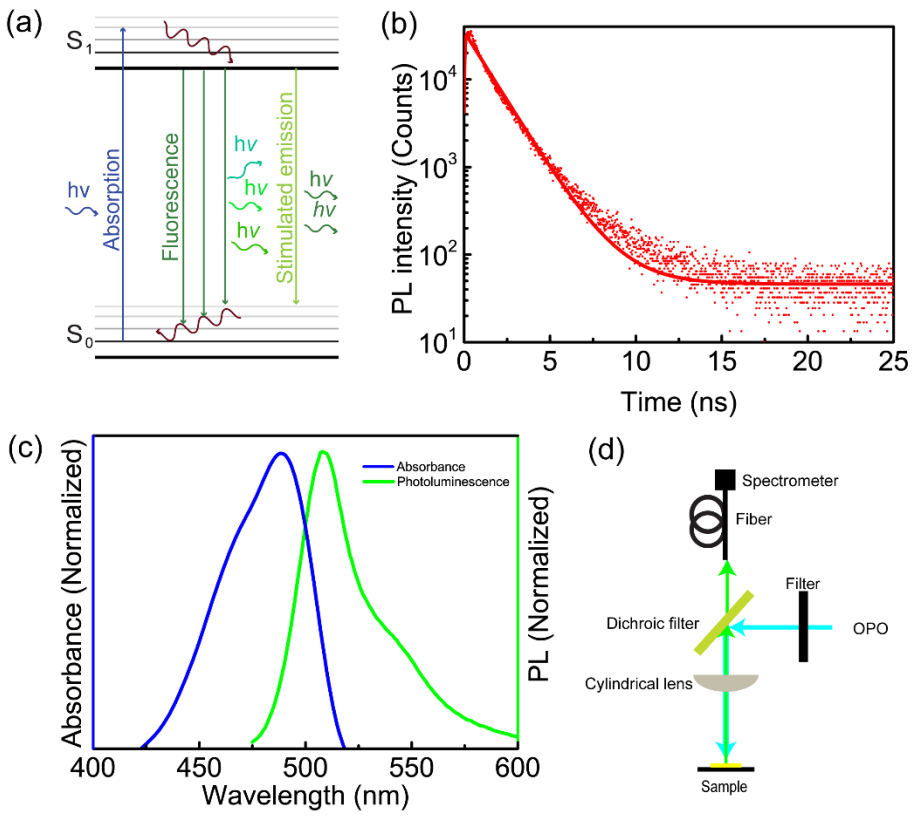

Figure 6.4 (a) Quasi-four-level energy diagram of eGFP with absorption, fluorescence and stimulated emission. **(b)** Time-resolved spectroscopy of 1:1 eGFP/silk at 520 nm that is spin-coated on glass. **(c)** Absorbance and photoluminescence spectrum of eGFP. **(d)** Schematic of the optical set-up for laser emission measurement.

When the laser structure using an all-protein gain medium is optically pumped, initially a broad emission is observed due to the dominance of spontaneous emission of eGFP with respect to the stimulated emission at low pumping levels (Figure 6.5-a). Above 92.1 $\mu J/mm^2$ a spectrally-narrow peak starts to be observed (Figure 6.5-b). Moreover, the slope efficiency above the threshold increases 12 times in comparison with below threshold (Figure 6.5-c). While the FWHM was around 24 nm below threshold, the FWHM reaches 1.1 nm above threshold, which is close to the resolution of our spectrometer (ca. 1 nm) (Figure 6.5-d). Furthermore, while the previous reports with fluorescent proteins present multi-mode laser emission due to the Fabry–Pérot and whispering gallery resonators [53, 64, 65], the distributed feedback cavity.

The threshold value of the protein laser is higher than the thresholds obtained from organic semiconductor DFB lasers and colloidal nanocrystal DFB lasers, which we attribute to the lower quantum yield of eGFP in solid form and scattering-induced losses due to random packing of proteins [65]. The reduction of the threshold can decrease the adverse effect of laser light generation in cellular environments (e.g., bleb formation due to photothermal effects [66]). In comparison with conventional lasers, protein lasers are advantageous in terms of their biocompatibility that allows them to be interfaced with biological environments. In addition, their biodegradation time may be also programmed such that they can be safely absorbed by the living system after the laser finishes its function [67]. These lasers can be used for intracellular sensing and light-generation [53, 68, 69].

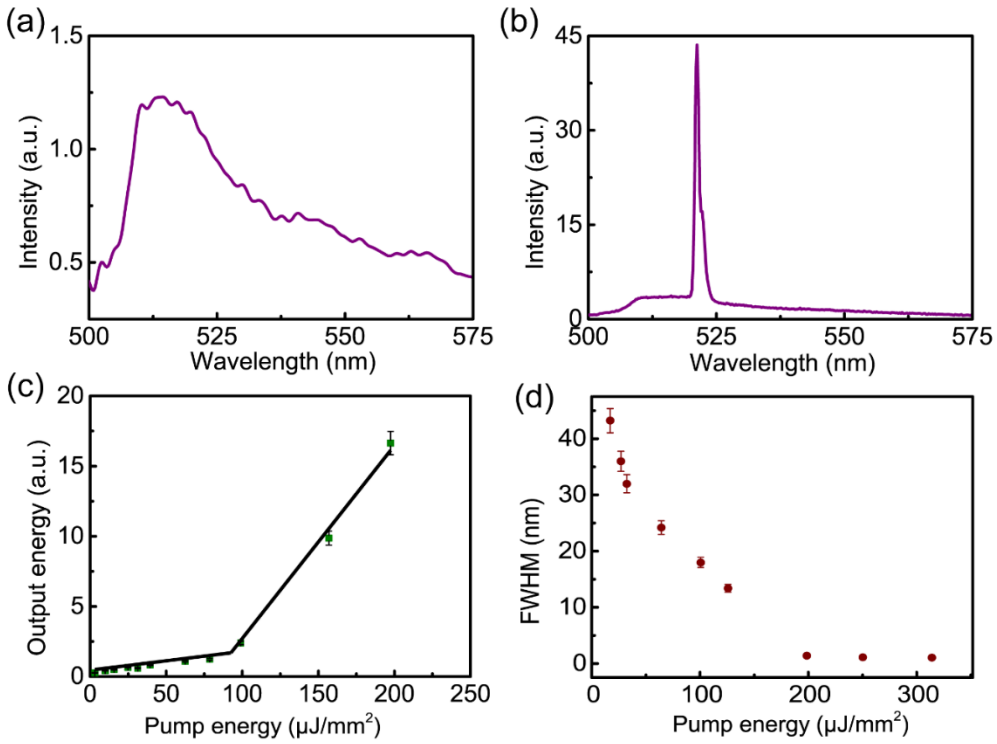

Figure 6.5 Emission spectra of spin coated 1:1 eGFP solution/SF solution **(a)** below **(b)** above threshold. **(c)** Measured light-light characteristic of the optically-pumped DFB laser. **(d)** FWHM of emission as a function of pump flux.

Chapter 7

CONCLUSION & FUTURE WORKS

In conclusion, we showed that the coffee stain effect is a useful, cost-effective, and facile method to fabricate the various type of self-assembled biolasers with small interventions. First, the effect of surface hydrophobicity and solution concentration is investigated. It is observed while hydrophilic surfaces lead to the formation of conventional 2D coffee stain, it has been demonstrated that superhydrophobic surfaces facilitate the formation of 3D coffee stain. Furthermore, spherical 3D coffee stains with excellent surface quality can be produced by the evaporation of a pendant droplet which leads to all-protein lasers. The spheres can further be modified with a wide variety of magnetic and optical nanomaterials to demonstrate novel free-standing devices by self-assembly. Furthermore, this study can open-up new scientific venues on the dynamics and modeling of interfacial interactions and investigations of unconventional 3D systems.

Then we analyzed the suppression of the coffee stain effect and obtained self-assembled disk biolasers. This method is suitable for mass production of disk lasers by using a wide variety of biomaterials. As a proof of concept, biomaterials such as SF and PVP were used as the construction material of the disk cavities, and organic dyes are used as the optical gain medium. By varying the size of the disks the laser emission wavelengths and thresholds can be controlled. Furthermore, the fabricated disks are flexible and detachable; even when they are bent or inserted on another surface, the disks show laser emission. Due to these properties, disk resonators can be integrated on different surfaces. Furthermore, it can be transferred as a building block in transient electronics and photonics for waste-free device production.

Following WGM cavities, we demonstrated self-assembled and directional random lasers using nano and biomaterial-based cracks. When the cracks were excited, the

rough side-facets scattered the luminescence generated by fluorophores and formed optical feedback for laser light generation. First, we created silica cracks, analyzed their mode, and in-plane directionality. Moreover, we showed the control of the output spectrum in terms of the spectral gain distribution. Following silica experiments, we exhibited that proteins and biopolymers can also function as RLs. We fabricated GFP and R6G doped PVP cracks and demonstrated random biolasers of cracks. In addition to the crack inside assemble, the random lasing was also observed from individual and free-standing pieces removed from the pattern through the crack boundaries.

Next, we demonstrated self-assembled directional random biolasers made of silk protein. We applied mechanical stress by folding and bending to the SF films that induced the nanocrack initiation and propagation along with the SF film. Thus, parallel nanocracks are formed and utilized as microcavities that support SLF based RL. The parallelism of the nanocracks allowed in-plane directional laser radiation. Advantageously, RLs can be produced with a facile, one-step, and cost-effective method. The directional random lasers hold great promise for integration to photonic circuits, and they can be interfaced with living systems for cell lasers and biosensors.

Last but not least, eGFP in a silk fibroin protein matrix was employed as an optical gain material for a DFB laser with a second-order grating fabricated on a quartz substrate with laser holography lithography. The laser holography lithography method was used to fabricate the large area grating that was designed according to the absorption and emission spectrum of eGFP. To provide strong optical feedback, a biocompatible TiO2 thin film was coated on the quartz grating. The spectral properties combined with the input-output energy relation reveals a single transverse mode protein laser. The biocompatibility of the biolaser holds promise for interfacing with biological cells or tissues that can be used for biosensing.

BIBLIOGRAPHY

[1] G. M. Whitesides and M. Boncheva, "Beyond molecules: Self-assembly of mesoscopic and macroscopic components," *Proceedings of the National Academy of Sciences,* vol. 99, no. 8, pp. 4769-4774, 2002.

[2] Z. Nie, D. Fava, E. Kumacheva, S. Zou, G. C. Walker, and M. Rubinstein, "Self-assembly of metal–polymer analogues of amphiphilic triblock copolymers," *Nature materials,* vol. 6, no. 8, pp. 609-614, 2007.

[3] N. Hano, M. Takafuji, and H. Ihara, "One-pot preparation of polymer microspheres having wrinkled hard surfaces through self-assembly of silica nanoparticles," *Chemical Communications,* vol. 53, no. 65, pp. 9147-9150, 2017.

[4] R. D. Deegan, O. Bakajin, T. F. Dupont, G. Huber, S. R. Nagel, and T. A. Witten, "Capillary flow as the cause of ring stains from dried liquid drops," (in English), *Nature,* vol. 389, no. 6653, pp. 827-829, Oct 23 1997.

[5] T. Breinlinger and T. Kraft, "A simple method for simulating the coffee stain effect," *Powder technology,* vol. 256, pp. 279-284, 2014.

[6] M. Zavelani-Rossi, M. G. Lupo, R. Krahne, L. Manna, and G. Lanzani, "Lasing in self-assembled microcavities of CdSe/CdS core/shell colloidal quantum rods," *Nanoscale,* vol. 2, no. 6, pp. 931-935, 2010.

[7] M. Zavelani-Rossi *et al.*, "Self-assembled CdSe/CdS nanorod micro-lasers fabricated from solution by capillary jet deposition," *Laser & Photonics Reviews,* vol. 6, no. 5, pp. 678-683, 2012.

[8] M. C. Gather and S. H. Yun, "Bio-optimized energy transfer in densely packed fluorescent protein enables near-maximal luminescence and solid-state lasers," *Nature communications,* vol. 5, p. 5722, 2014.

[9] F. L. Pedrotti, L. M. Pedrotti, and L. S. Pedrotti, *Introduction to optics*. Cambridge University Press, 2017.

[10] S. O. Kasap, *Optoelectronics & Photonics: Principles & Practices: International Edition*. Pearson Higher Ed, 2013.

[11] A. Sennaroglu, *Photonics and laser engineering: principles, devices, and applications*. McGraw-Hill, 2010.

[12] M. Gomilšek, "Whispering gallery modes," *Univ. Ljubl. Ljubl. Semin,* vol. 11, 2011.

[13] H. Cao, "Random lasers: development, features and applications," *Optics and photonics news,* vol. 16, no. 1, pp. 24-29, 2005.

[14] H. Cao *et al.*, "Random lasers with coherent feedback," *IEEE Journal of selected topics in quantum electronics*, vol. 9, no. 1, pp. 111-119, 2003.

[15] D. S. Wiersma, "The physics and applications of random lasers," *Nature physics*, vol. 4, no. 5, p. 359, 2008.

[16] H. Cao, Y. Zhao, S. Ho, E. Seelig, Q. Wang, and R. Chang, "Random laser action in semiconductor powder," *Physical Review Letters*, vol. 82, no. 11, p. 2278, 1999.

[17] C. Gollner *et al.*, "Random lasing with systematic threshold behavior in films of CdSe/CdS core/thick-shell colloidal quantum dots," *ACS nano*, vol. 9, no. 10, pp. 9792-9801, 2015.

[18] A. Consoli and C. Lopez, "Emission regimes of random lasers with spatially localized feedback," *Optics express*, vol. 24, no. 10, pp. 10912-10920, 2016.

[19] P. Aramwit, "Introduction to biomaterials for wound healing," in *Wound healing biomaterials*: Elsevier, 2016, pp. 3-38.

[20] D. N. Rockwood, R. C. Preda, T. Yucel, X. Q. Wang, M. L. Lovett, and D. L. Kaplan, "Materials fabrication from Bombyx mori silk fibroin," (in English), *Nature Protocols*, vol. 6, no. 10, pp. 1612-1631, Oct 2011.

[21] Y. Qi *et al.*, "A review of structure construction of silk fibroin biomaterials from single structures to multi-level structures," *International journal of molecular sciences*, vol. 18, no. 3, p. 237, 2017.

[22] H. Perry, A. Gopinath, D. L. Kaplan, L. Dal Negro, and F. G. Omenetto, "Nano-and micropatterning of optically transparent, mechanically robust, biocompatible silk fibroin films," *Advanced Materials*, vol. 20, no. 16, pp. 3070-3072, 2008.

[23] Y. Cheng, L.-D. Koh, D. Li, B. Ji, M.-Y. Han, and Y.-W. Zhang, "On the strength of β-sheet crystallites of Bombyx mori silk fibroin," *Journal of the Royal Society Interface*, vol. 11, no. 96, p. 20140305, 2014.

[24] R. M. Hoffman, "Green fluorescent protein imaging of tumour growth, metastasis, and angiogenesis in mouse models," *The lancet oncology*, vol. 3, no. 9, pp. 546-556, 2002.

[25] M. A. Rizzo, M. W. Davidson, and D. W. Piston, "Fluorescent protein tracking and detection: fluorescent protein structure and color variants," *Cold Spring Harbor Protocols*, vol. 2009, no. 12, p. pdb. top63, 2009.

[26] I. B. Dogru *et al.*, "Single transverse mode protein laser," *Applied Physics Letters*, vol. 111, no. 23, p. 231103, 2017.

[27] D. A. Press, R. Melikov, D. Conkar, E. N. Firat-Karalar, and S. Nizamoglu, "Fluorescent protein integrated white LEDs for displays," *Nanotechnology*, vol. 27, no. 45, p. 45LT01, 2016.

[28] SpectraPhysics. *Quanta-Ray INDI*. Available: https://www.spectra-physics.com/products/high-energy-pulsed-lasers/quanta-ray-indi

[29] SpectraPhysics. *basiScan*. Available: https://www.spectra-physics.com/products/high-energy-pulsed-lasers/basiscan

[30] ANDOR. *Oxford Instruments*. Available: https://andor.oxinst.com/products/kymera-and-shamrock-spectrographs/shamrock-500i#product-information-tabs

[31] I. B. Dogru *et al.*, "3D coffee stains," *Materials Chemistry Frontiers*, vol. 1, no. 11, pp. 2360-2367, 2017.

[32] E. Y. Cagla Kosak Soz, Iskender Yılgor, "Influence of the coating method on the formation of superhydrophobic silicone-urea surfaces modified with fumed silica nanoparticles " *Progress in Organic Coatings* vol. 84, pp. 143-152, 2015.

[33] R.-H. Chen, T. X. Phuoc, and D. Martello, "Effects of nanoparticles on nanofluid droplet evaporation," *International Journal of Heat and Mass Transfer*, vol. 53, no. 19, pp. 3677-3682, 2010.

[34] J. Zhang *et al.*, "Surface energy of silk fibroin and mechanical properties of silk cocoon composites," (in English), *Rsc Advances*, vol. 5, no. 2, pp. 1640-1647, 2015.

[35] Y. Li, Q. Yang, M. Li, and Y. Song, "Rate-dependent interface capture beyond the coffee-ring effect," *Scientific reports*, vol. 6, 2016.

[36] I. B. Dogru, R. Melikov, and S. Nizamoğlu, "Biomaterial Disk Lasers by Suppressing the Coffee Ring Effect," *ACS Biomaterials Science & Engineering*, 2018.

[37] S. Kim, A. N. Mitropoulos, J. D. Spitzberg, H. Tao, D. L. Kaplan, and F. G. Omenetto, "Silk inverse opals," *Nature Photonics*, vol. 6, no. 12, pp. 818-823, 2012.

[38] Y. Jin *et al.*, "Buckled Au@ PVP nanofiber networks for highly transparent and stretchable conductors," *Advanced Electronic Materials*, vol. 2, no. 2, 2016.

[39] S. Kim *et al.*, "All-water-based electron-beam lithography using silk as a resist," *Nature nanotechnology*, vol. 9, no. 4, p. 306, 2014.

[40] F. Vollmer and S. Arnold, "Whispering-gallery-mode biosensing: label-free detection down to single molecules," *Nature methods*, vol. 5, no. 7, p. 591, 2008.

[41] T.-S. Wong, T.-H. Chen, X. Shen, and C.-M. Ho, "Nanochromatography driven by the coffee ring effect," *Analytical chemistry*, vol. 83, no. 6, pp. 1871-1873, 2011.

[42] S. K. Tang, R. Derda, Q. Quan, M. Lončar, and G. M. Whitesides, "Continuously tunable microdroplet-laser in a microfluidic channel," *Optics express*, vol. 19, no. 3, pp. 2204-2215, 2011.

[43] A. Francois and M. Himmelhaus, "Optical sensors based on whispering gallery modes in fluorescent microbeads: Size dependence and influence of substrate," *Sensors*, vol. 9, no. 9, pp. 6836-6852, 2009.

[44] H. Ma and J. Hao, "Ordered patterns and structures via interfacial self-assembly: superlattices, honeycomb structures and coffee rings," *Chemical Society Reviews*, vol. 40, no. 11, pp. 5457-5471, 2011.

[45] J. Y. Kim, K. Cho, S.-a. Ryu, S. Y. Kim, and B. M. Weon, "Crack formation and prevention in colloidal drops," *Scientific reports*, vol. 5, p. 13166, 2015.

[46] K. B. Singh and M. S. Tirumkudulu, "Cracking in drying colloidal films," *Physical review letters*, vol. 98, no. 21, p. 218302, 2007.

[47] M. Naqshbandi, J. Canning, B. C. Gibson, M. M. Nash, and M. J. Crossley, "Room temperature self-assembly of mixed nanoparticles into photonic structures," *Nature communications*, vol. 3, p. 1188, 2012.

[48] W. Han, B. Li, and Z. Lin, "Drying-mediated assembly of colloidal nanoparticles into large-scale microchannels," *ACS nano*, vol. 7, no. 7, pp. 6079-6085, 2013.

[49] J. H. Prosser, T. Brugarolas, S. Lee, A. J. Nolte, and D. Lee, "Avoiding cracks in nanoparticle films," *Nano letters*, vol. 12, no. 10, pp. 5287-5291, 2012.

[50] I. Malitson, "Interspecimen comparison of the refractive index of fused silica," *Josa*, vol. 55, no. 10, pp. 1205-1209, 1965.

[51] Q. Song, S. Xiao, Z. Xu, V. M. Shalaev, and Y. L. Kim, "Random laser spectroscopy for nanoscale perturbation sensing," *Optics letters*, vol. 35, no. 15, pp. 2624-2626, 2010.

[52] P. J. Yunker, T. Still, M. A. Lohr, and A. Yodh, "Suppression of the coffee-ring effect by shape-dependent capillary interactions," *Nature*, vol. 476, no. 7360, pp. 308-311, 2011.

[53] M. C. Gather and S. H. Yun, "Single-cell biological lasers," *Nature Photonics*, vol. 5, no. 7, p. 406, 2011.

[54] H. J. Oh, M. C. Gather, J.-J. Song, and S. H. Yun, "Lasing from fluorescent protein crystals," *Optics express*, vol. 22, no. 25, pp. 31411-31416, 2014.

[55] M. Ormo, A. B. Cubitt, K. Kallio, L. A. Gross, R. Y. Tsien, and S. J. Remington, "Crystal structure of the Aequorea victoria green fluorescent protein," (in eng), *Science*, vol. 273, no. 5280, pp. 1392-5, Sep 6 1996.

[56] A. Consoli and C. López, "Decoupling gain and feedback in coherent random lasers: experiments and simulations," *Scientific reports,* vol. 5, p. 16848, 2015.

[57] Lumerical. *Bidirectional scattering distribution function (BSDF)*. Available: https://support.lumerical.com/hc/en-us/articles/360042213854-Bidirectional-scattering-distribution-function-BSDF-

[58] S. Caixeiro, M. Gaio, B. Marelli, F. G. Omenetto, and R. Sapienza, "Silk-based biocompatible random lasing," *Advanced Optical Materials,* vol. 4, no. 7, pp. 998-1003, 2016.

[59] M. Umar, K. Min, S. Kim, and S. Kim, "Random lasing and amplified spontaneous emission from silk inverse opals: Optical gain enhancement via protein scatterers," *Scientific reports,* vol. 9, 2019.

[60] S. Yang *et al.*, "Random lasing detection of structural transformation and compositions in silk fibroin scaffolds," *Nano Research,* pp. 1-9, 2018.

[61] M. V. Santos *et al.*, "Silk fibroin as a biotemplate for hierarchical porous silica monoliths for random laser applications," *Journal of Materials Chemistry C,* vol. 6, no. 11, pp. 2712-2723, 2018.

[62] V. Passaro and M. La Notte, "Optimizing SOI slot waveguide fabrication tolerances and strip-slot coupling for very efficient optical sensing," *Sensors,* vol. 12, no. 3, pp. 2436-2455, 2012.

[63] B. C. J. Zoeteman, H. R. Krikke, and J. Venselaar, "Handling WEEE waste flows: on the effectiveness of producer responsibility in a globalizing world," (in English), *International Journal of Advanced Manufacturing Technology,* vol. 47, no. 5-8, pp. 415-436, Mar 2010.

[64] C. P. Dietrich *et al.*, "An exciton-polariton laser based on biologically produced fluorescent protein," (in English), *Science Advances,* vol. 2, no. 8, Aug 2016.

[65] B. H. Robinson, "E-waste: An assessment of global production and environmental impacts," (in English), *Science of the Total Environment,* vol. 408, no. 2, pp. 183-191, Dec 20 2009.

[66] S. Nizamoglu *et al.*, "A Simple Approach to Biological Single-Cell Lasers Via Intracellular Dyes," *Advanced Optical Materials,* 2015.

[67] S. Nizamoglu *et al.*, "Bioabsorbable polymer optical waveguides for deep-tissue photomedicine," *Nature communications,* vol. 7, 2016.

[68] M. Humar and S. H. Yun, "Intracellular microlasers," *Nature Photonics,* 2015.

[69] M. C. Gather and S. H. Yun, "Lasing from Escherichia coli bacteria genetically programmed to express green fluorescent protein," *Optics letters*, vol. 36, no. 16, pp. 3299-3301, 2011.